TECHNISCHE
UNIVERSITÄT
WIEN
Vienna University of Technology

DIPLOMARBEIT

Development of a Testing and Simulation Protocol for Proximal Femurs

ausgeführt zum Zwecke der Erlangung
des akademischen Grades eines Diplom-Ingenieur
unter der Leitung von

Privatdoz. Dipl.-Ing. Dr. techn. Dieter H. Pahr

Institut für Leichtbau und Struktur-Biomechanik (E317)

eingereicht an der Technischen Universität Wien
Fakultät für Maschinenwesen und Betriebswissenschaften

von

Bernhard Fritz
E700/e0326461
Josef Schöffelg. 5
3021 Pressbaum

Wien, im Juni 2010

Abstract

Hip fractures due to osteoporosis are an important issue in health care. They are not only a financial burden on the Austrian health care system, that cost €1.7 billion a year, but are also severe injuries for the concerned persons. Patients, who are assessed of having a high fracture risk can be medicated with preventive drug treatments. Currently, clinical diagnosis of osteoporosis is based on BMD analysis, which is limited due to its inability to take the three-dimensional structure of the bone into account. Alternatively, the QCT-image based three-dimensional finite element (FE) models showed promising results, but need to be validated through experimental tests in vitro. The goal of this thesis was to do a feasibility study containing the basic procedures, that would be needed in a subject-specific validation study. Therefore, a CT-imaging chamber, a testing setup, and an FE-model were developed. Three pairs of proximal femurs were scanned in a QCT scanner and were tested up to the point of failure. Two loading scenarios were considered. A fall to the side (fall configuration) and a "spontaneously" occurring fracture due to joint loading during daily activities (stance configuration). A motion-capture system was used to measure local movements of the femurs and the testing setup. FE-models with non-linear material behavior were generated from the QCT-images, and compared to the experiments.

The CT-imaging chamber as well as the testing setup were found to fulfill the requirements. Fractures were induced and fracture load and compliance of the femurs were measured, beeing in the same order of magnitude of previous results. Fracture location was qualitatively well predicted in the stance configuration. Local movements could qualitatively well be predicted in both configurations. Finally, possible improvements concerning both the testing setup and the FE-models were examined and discussed.

Kurzfassung

Durch Osteoporose verursachte Hüftbrüche kosten dem österreichischen Gesundheitswesen €1, 7 Milliarden pro Jahr und stellen außerdem für die Patientin/den Patienten ein schwerwiegendes gesundheitliches Problem dar. Diagnostiziert man bei Patienten ein erhöhtes Hüftbruchrisiko, so ist man in der Lage, diese Patienten medikamentös zu behandeln, um das Risiko zu senken. Momentan basiert die klinische Diagnose von Osteoporose auf BMD-Analysen, die jedoch nicht die dreidimensionale Knochenstruktur erfassen können. Andererseits zeigten QCT-basierte, dreidimensionale Finite-Elemente (FE) Modelle viel versprechende Resultate, die allerdings experimentell validiert werden müssen („in-vitro"-Validierung). Das Ziel dieser Diplomarbeit war eine Machbarkeitsstudie durchzuführen, um die wichtigsten Aspekte, die für die Durchführung einer fallspezifischen Validierungsstudie notwendig sind, zu beleuchten: Konkret wurde eine CT-Kammer, ein Versuchsstand, ein Versuchsprotokoll und ein FE-Modell entwickelt. Es wurden drei proximale Femurpaare in einem QCT gescannt, um diese dann in experimentellen Versuchen bis zum Bruch zu belasten. Dabei wurden zwei Lastfälle getestet: Ein seitlicher Fall und ein Hüftbruch, hervorgerufen durch auftretende Gelenkkräfte in täglichen Aktivitäten (Standbruch). Mittels eines optischen Messsystems konnten lokale Verschiebungen der Femura und des Versuchsaufbaus gemessen werden. Unter Verwendung der QCT-Bilder wurden FE-Modelle mit nicht-linearen Materialeigenschaften generiert und deren Ergebnisse mit den Experimenten verglichen.
Sowohl die CT-Kammer als auch der Versuchsstand genügte den Anforderungen. Die auftretenden Bruchkräfte und Steifigkeiten der Femura waren von der gleichen Größenordnung wie Resultate vergleichbarer Studien. Die Bruchstellen des Standbruchs wurden qualitativ gut berechnet. Lokale Verschiebungen der Femura konnten qualitativ für beide Lastfälle vorhergesagt werden. Schließlich wurden mögliche Verbesserungen des Versuchsstandes und der FE-Modelle untersucht und diskutiert.

Contents

1 General Introduction

1.1 Bone Tissue

The human skeletal system is an exceptional structure, consisting of 206 bones in the average adult and the connective tissue that joins them. Bones are the main component of the system, being both biomechanically (due to its hardness and rigidity) and metabolically important to the human body. They are serving many functions, including:

- maintaining the shape of the body
- protecting the soft tissues of the cranial, thoracic, and pelvic cavities
- supplying the framework for the bone marrow, which produces blood cells and stem cells
- transferring muscle force by giving muscles points of application and by bringing forward the force
- acting as a reservoir for Ca^{2+}

Since bone is a living, dynamic, self repairing tissue, it is constantly being renewed. Estimated 10-15% of the bone in the whole body of a healthy subject is replaced with new bone every year [51]. It is able to adapt its mass, shape, and properties to its mechanical environment.

Looking at bone tissue, one can differentiate between *cortical* and *trabecular* bone (Figure 1.1). The primary difference between these two bone types is their porosity. To make this differentiation, *apparent density* first needs to be defined, which is mass divided by bulk volume. Apparent mechanical properties are the properties of bone on a scale $> 1\,\mathrm{mm}$. The apparent density of solid cortical bone is approximately $1.8\,\mathrm{g/cm^3}$ [18]. The *relative density* is defined as the ratio of the apparent density of a specimen to that of solid cortical bone. A bone specimen with a relative density > 0.7 is considered as cortical bone, while trabecular bone is defined as a bone with a relative density < 0.7, corresponding to a porosity of $30\,\%$ [53]. However, porosity of trabecular bone can be much lower, approaching values of up to $95\,\%$.

Cortical (compact) bone is dense and solid, with only microscopic channels (Haversian canal and Volkmann's canal) . Approximately 80% of the skeletal mass in the adult human skeleton is cortical bone [11]. It covers the outer surface of most bones, but it is also found in the shafts of the long bones (e.g. femur). Due to its low porosity, cortical bone is responsible for the supportive and protective function of the skeleton.

Trabecular (cancellous, spongy) bone consists of a three-dimensional porous network of interconnected struts called trabeculae, which on average are about 200 μm thick in healthy bone [11]. Like cortical bone, it consists of a lamellar structure, having lamellae, which are parallel to the trabeculae. The pores between trabeculae are filled with bone marrow. Due to its higher porosity, trabecular bone is much lighter than cortical bone. It is found in the vertebrae and in the epiphyses of the long bones, such as femur, tibia, and radius. Age-related fractures primarily occur at trabecular bone sites (e.g. proximal femur/hip). Loss of bone mass comes along with fewer and thinner trabeculae for osteoporosis. Cancellous bone material is much more metabolically active, is remodeled more often, and is, therefore, "younger" on average than cortical bone [25].

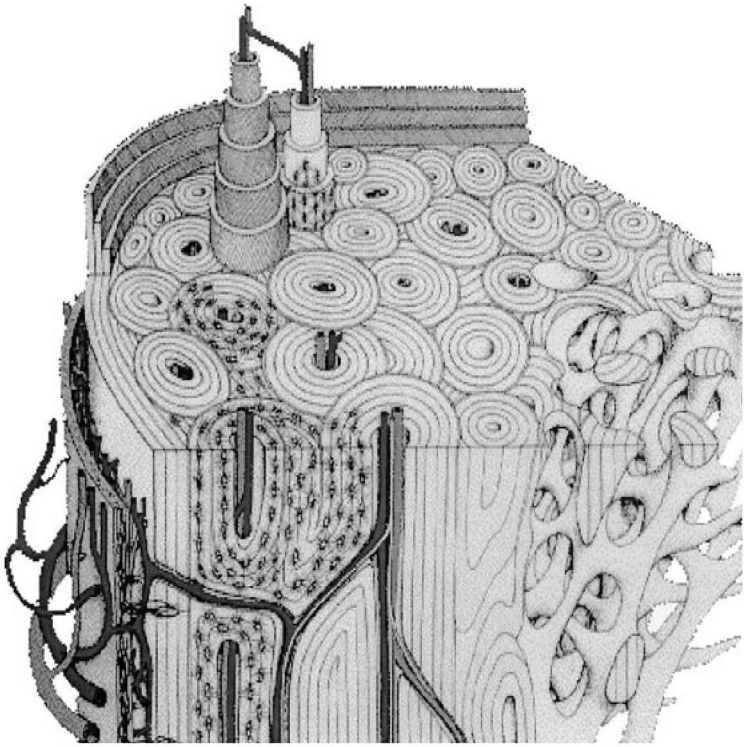

Figure 1.1: Schematic drawing illustrating the architecture of cortical and trabecular bone. From Einhorn et al. [17].

1.1.1 Biomechanical Properties of Cortical and Trabecular Bone

Cortical bone is anisotropic. Stiffness and strength in longitudinal direction are greater than properties transverse to the bone axis. Moreover, cortical bone is stronger in compression than in tension. A summary of mechanical properties of human cortical bone is shown in Table 1.1.

For trabecular bone, the apparent properties are strongly dependent on the relative density and architecture, which vary with anatomic site and age and can be influenced by hormone-related diseases. Statistical analyses of experimental results show that both Young's modulus and compressive strength of cancellous bone tissue are strongly dependent on apparent density and have a weak dependency on strain rate. They can be described by a power law function of the formula

$$\sigma_{\text{ult}} \propto \dot{\epsilon}^a \rho^b \,, \tag{1.1}$$

$$E \propto \dot{\epsilon}^a \rho^b \,, \tag{1.2}$$

where the parameter b is ranging between 2 and 3 [26, 55] and $a \approx 0.06$ for strain rates in the physiological range of 0.001-0.03 s^{-1}, being greater at higher strain rates [18].

There is another interesting aspect concerning the non-elastic apparent behavior of bone. If bone is loaded above its elastic regime, its behavior can be explained by two distinct modes of deformation, which are damage and plastic. Damage is related to energy dissipation and residual strains due to microcracks. The plastic regime corresponds to unloading and reloading of the damaged structure and may be a result of microcracks sliding [63]. Figure 1.2 explains this behavior by showing the strain-stress curves of quasi-static cycling loading of trabecular and cortical bone.

1.1.2 The Change of Skeletal Mass

Bone adapts to changes in mechanical requirements. As a result, a reduction in physical activity leads to decreased bone density. However, bone mass does not only vary because of disuse or other causes, like hormone-related diseases. It is also related to age: Bone mass rises during growth, is followed by a peak and with increasing age, people, particularly postmenopausal women, start to lose bone mass (Figure 1.3). At the age of 70, less than 70% can remain [11]. This bone loss can result in osteoporosis, whereas 80% of the affected people are women [11]. Osteoporosis is defined by The World Health Organization as a *Bone Mineral Density, that is over 2.5 standard deviations below the mean value for young adults.*

Table 1.1: Mechanical properties of cortical bone tissue

Parameter	Value
Modulus [GPa]	
Longitudinal	17.0
Transverse	11.5
Shear	3.3
Poisson's ratio	0.3-0.6
Ultimate strength: longitudinal (MPa)	
Tension	133
Compression	193
Shear	68
Ultimate strength: transverse (MPa)	
Tension	51
Compression	133

From Reilly and Burstein [54]

Bone mineral density (BMD) is derived from the amount of scanned mineral, divided by the area (aBMD in g/cm^2) or volume (vBMD in g/cm^3). Since Young's modulus and the strength of cancellous bone tissue are strongly dependent on the apparent density (Equation 1.2), fracture risk increases with the decrease of bone mass. It is estimated that up to 40% of women over the age of 50 will have an osteoporosis-related fracture in their lifetime [11].

1.1.3 Geometry of Femur and Hip

Since bones exist in various shapes and sizes, one can roughly differentiate them into long, short, flat and irregular bones. A typical long bone like femur, humerus or tibia, consists of a central cylindrical shaft (diaphysis) and two wider and rounded ends, the epiphyses, which have joints covered by articular cartilage to carry equal loads. The metaphysis connects the diaphysis with each epiphysis. The epiphysis and metaphysis consist mostly of cancellous bone with a thin cortical shell. As a contrast, the diaphysis is made mainly of cortical bone that surrounds cancellous tissue and a medullary canal, which contains marrow. Most biomechanical publications dealing with prediction of femur-related fractures only investigate the proximal part of the femur, since this is the part where most osteoporosis-related fractures

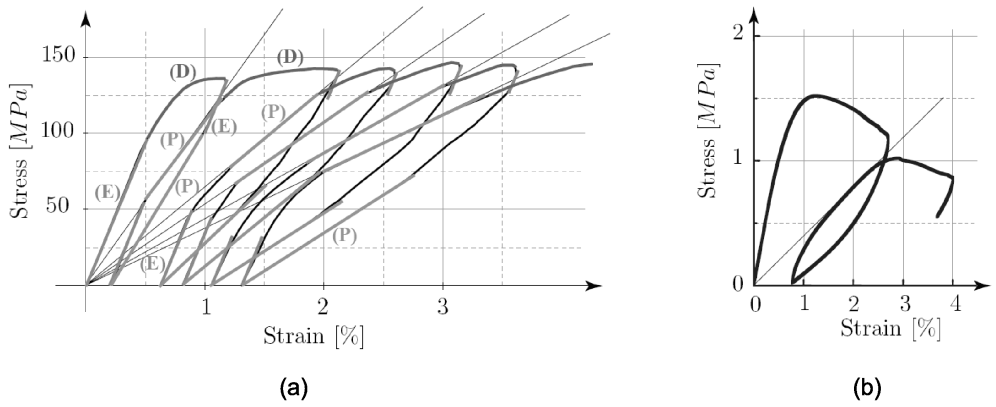

Figure 1.2: Stress-strain curves of a quasi-static cycling loading in tension for: (a) cortical bone, showing the different states of deformation: (E) intact linear elastic mode, (D) damage mode, and (P) plastic mode (adopted from Garcia [21]) and (b) trabecular bone, which can be described with the same deformation modes (adapted from Keaveny et al. [30]).

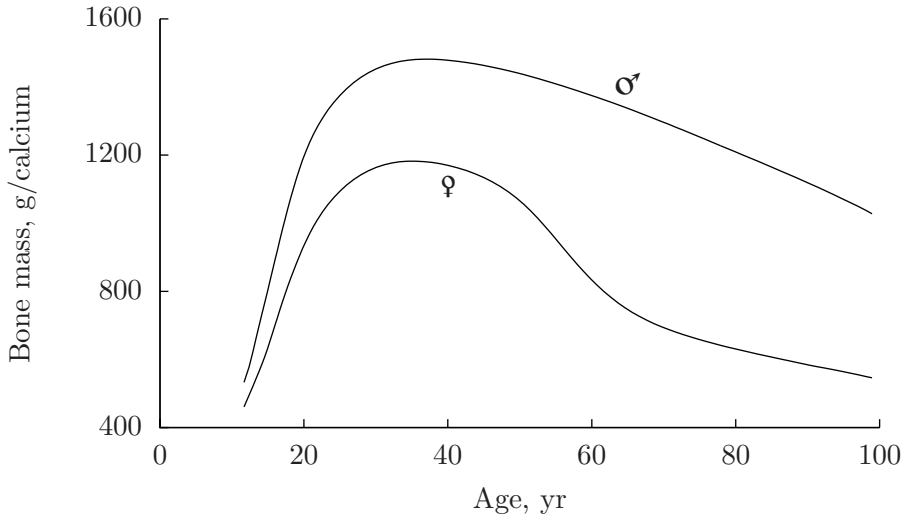

Figure 1.3: Age-related bone loss throughout life. Loss of bone begins approximately 10 years earlier and proceeds approximately twice as fast in women as in men [11]. Adapted from Riggs and Melton [57]

occur. Figure 1.4 shows some relevant terms that describe the shape and geometry of femurs, Table 1.2 summarizes dimensions, which can be found in the literature.

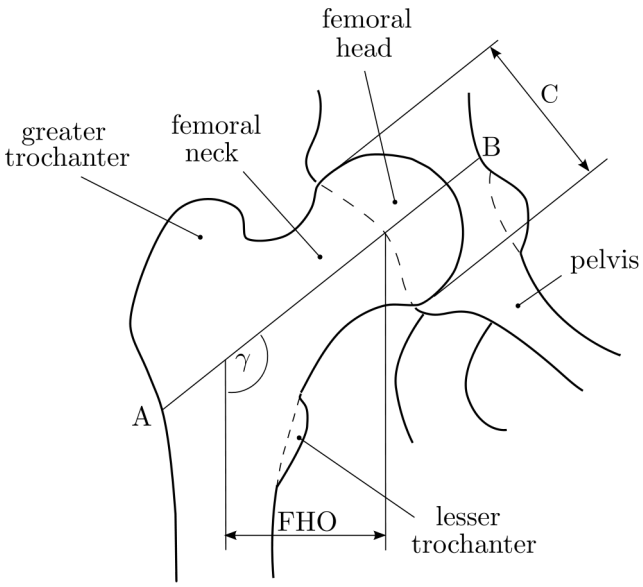

Hip Axis Length (HAL)	AB
Femoral Head Diameter	C
Femoral Head Offset	FHO
Neck Shaft Angle	γ

Figure 1.4: Geometry of hip joint demonstrating some of the most common measurements and anatomical terms of the proximal femur. Corresponding values are shown in table 1.2.

1.1.4 Hip Fractures

There are several different classifications for hip fractures. In this work, the AO classification of Müller [47] will be used to describe the femoral fractures (Figure 1.5).

To induce femoral fractures in vitro, it is necessary to define the applied loading conditions. Therefore, it is important to know the history of the fracture origins. Basically, there are two fracture scenarios of proximal femurs that have been investigated in a biomechanical context so far: (1) traumatic femoral fracture due to impact on the greater trochanter as

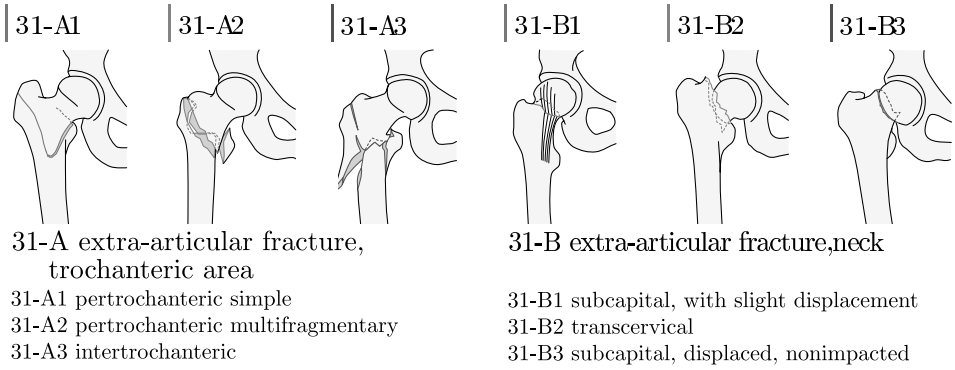

Figure 1.5: AO classification of femoral trochanteric and neck fractures (Copyright by AO Publishing, Switzerland).

Table 1.2: Mean values of basic femoral geometry.

Parameters	Mean	±	SD	Range
Hip Axis length[b] [mm]	130.5	±	8.9	-
Femoral Head Diameter[a] [mm]	43.4	±	2.6	39.3 to 48.3
Femoral Head Offset[a] [mm]	47.0	±	7.2	33.2 to 62.8
Neck Shaft Angle[a] [°]	122.9	±	7.6	100.7 to 137.8

[a] Rubin et al. [59]: The results for anteroposterior radiographic measurements (n=32)

[b] Calis et al. [5]: The results for bilateral radiographic measurements of cases with no hip fractures (n=232)

a consequence of sideways fall, and (2) a "spontaneously" occurring fracture due to joint loading during daily activities ("one-leg stance"). Both have been extensively investigated in vitro. However, in both load cases, different loading scenarios were applied, since there is no agreement concerning the critical load configurations to be simulated: In the one-leg stance configuration, the direction of the force applied to the femoral head varies from 0° [44, 42] to 20° [35, 40], and to 25° [9] relative to the shaft axis. In the fall scenario, most groups apply the load 60° relative to the shaft axis [35, 43, 40], but also 80° were applied [48, 10]. The orientation of the neck axis is not as clear: Some groups rotated the femoral neck internally 15° (that is approximately 15° to the load axis) [48, 10, 66]), others define the exact angle between loading axis and femoral neck axis from 60° [43] to 70° [35, 40].

Another unclear point is the relevance of muscle force, which is neglected by most investigations. Amongst others, Cristofolini et al. [12] investigated that question by using a detailed, density-based, inhomogeneous continuum finite element model [61] and came to the conclusion that exclusion of muscle force tends to slightly overestimate the risk of fracture. However, to the author's knowledge there are no existing experimental results concerning this question.

Hip fracture due to osteoporosis is an important issue in health care. In Austria, approximately 16,500 people suffer a hip fracture each year [16]. Thus, Austria's rate of 19.7 hip fractures per 10,000 inhabitants over the age of 65 is one of the highest in Europe [16]. Medical care and rehabilitation for hip fractures in Austria do not only cost €1.7 billion a year [15], but also the consequence for each affected person is severe. Half of all the people who were fully mobile before an osteoporotic hip fracture suffer permanent restricted mobility following a hip fracture [16]. An analysis of Austrian hospital data from 1995 (published

2001) showed that 6.8% of all patients with osteoporotic hip fractures died during hospitalization [38]. These numbers lead to the importance of preventing hip fractures. Preventive measures could be taken if there were inexpensive and accurate tests to identify the fracture risk of patients.

The definition of osteoporosis leads to the current gold standard for osteoporosis diagnosis, which is dual energy X-ray absorptiometry (DXA) of the femoral neck.

1.2 Imaging Procedures for Femoral Geometry

Possible imaging methods include DXA, the quantitative computed tomography (QCT), and the high resolution peripheral quantitative computed tomography (HR-pQCT). Neither DXA nor the QCT account for the microarchitecture of bone tissue. QCT is used to measure vBMD (ρ_{QCT}), while DXA is two-dimensional and can only be used to measure aBMD. In contrast, HR-pQCT is not only three-dimensional, but is also able to describe the microarchitecture of bone [39, 45].

DXA is currently the most commonly used method to screen patients at risk for osteoporosis and hip fractures. Its pros are low cost and low radiation, but its output is the two-dimensional value aBMD. This means that the bone dimensions affect the BMD-value only indirectly, resulting in larger bones having a higher aBMD due to their increased thickness [1]. Nonetheless, DXA images allow to extract geometric parameters, which might be a useful addition to BMD. Hip Axis Length (HAL, see Figure 1.4), for example, is related to an increased fracture risk [24], which was first shown by Faulkner et al. [20] in the Study of Osteoporotic Fractures in 1993. Biomechanically, the link between HAL and fracture risk is intuitive. A longer HAL results in a greater bending moment in the femoral neck in a fall on the greater trochanter, when weight of the falling body is applied through the femoral head, making it more likely to fracture [24].

QCT, on the other hand, has the advantage of being three-dimensional and measuring vBMD, but requires longer scan times, a more specialized equipment, and a high patient X-ray dose.

Cody et al. [9] investigated the ability of DXA (5 areal densities) and QCT (three volumetric cancellous densities and three dimensions) to predict the fracture load, which was also measured experimentally at a one-leg stance configuration. As a result, they got $R^2 = 0.57$ and $R^2 = 0.66$ for the prognosis of strength from DXA and QCT, respectively, suggesting

that DXA or QCT measurements were not reliable for predicting femoral strength in clinical settings.

Attempting to improve prediction of fracture risk, the epidemiology-based questionnaire (FRAX, http://www.shef.ac.uk/FRAX) [29] includes the femoral neck BMD and additional clinical risk factors to predict the fracture risk tor the next 10 years for a patient. Those risk factors comprise the body mass index (BMI), a prior history of fracture, a parental history of hip fracture etc. It is still unknown to what extent the results of this questionnaire are reliable.

HR-pQCT share the mentioned disadvantages of the QCT. They require even longer scan times and more specialized equipment. Additionally, HR-pQCT scans can presently only be taken of parts of the peripheral skeleton. However, HR-pQCT-scans have the great benefit of representing the microarchitecture, what can improve the prediction potential of finite element models.

1.3 Finite Element Method

The finite element (FE) analysis includes three-dimensional geometry, material properties and loading conditions and can, therefore, be used as a better predictor of femoral strength than the so-far presented methods [9].

Brekelmans et al. [3] were the first who used the FE analysis in orthopedic biomechanics [19]. In 1972 they evaluated the mechanical behavior of a femur with a two-dimensional model in different load situations.

Today, FE models are standard computational tools for analyzing the mechanical properties of bones. There are two major bone-model types mentioned in literature: *continuum-level* models [36, 69, 61, 2, 9, 68] and *micro FE* models [66, 56].

1.3.1 Continuum-Level Models

Continuum-level models are used in case of limited image resolutions, that is usually in clinical applications. In these models, the element stiffness is a function of the bone density, which is obtained from the QCT scan. The QCT is not able to capture the trabecular architecture and, thus, the bone anisotropy. That is why most studies describe bone tissues as isotropic (amongst other studies mentioned in the paragraph before). Another limitation is the simplistic modeling of the cortical shell: FE models generated directly from QCT

images are homogenized, since averaging of the densities is done inherently during scanning. The voxel size is in the same order of magnitude as the cortex thickness, which prevents a reliable modeling of the cortical shell.

Another challenge is the need for a relationship between the density values obtained by the CT-scan and element stiffness. One example is given in the Equation 1.2 by Rice et al. [55], but there are many different relationships proposed in literature (e.g. [31, 34, 6, 41, 46]).

However, despite the mentioned limitations, the FE based predictions of bone strength seem to be more reliable than using DXA or QCT to predict femoral strength. Cody et al. [9] reported good results using a FE-model without including the cortical shell and where the computed spring stiffness was used as a predictor for fracture load. They stated that the FE-method ($R^2 = 0.84$) explains 20% more of the variance than the DXA model. Their choice of selecting the spring stiffness as a predictor was based on empirical evidence that showed a strong relationship between elastic modulus and ultimate stress for cancellous and cortical bone samples obtained from many anatomical sites [23]. Additionally, they referred to the work of Jurist and Foltz [27], who showed a strong correlation between bone stiffness and strength for the human ulna ($R = 0.958$). However, fracture load was also predicted directly by other research groups, using nonlinear FE methods. Keyak [33], for instance, explained 93% of the variance in fracture load in a stance configuration.

1.3.2 Micro FE Models

By using high-resolution Micro FE (μFE) models, one can avoid some of the above described problems: Such a model can represent the trabecular structure in detail and represents the cortical shell automatically. It accounts for bone anisotropy by converting the voxels that represent bone tissue to equally shaped 8-noded brick elements (e.g. [62, 56, 67]). Thus, it does not require any relationship to translate bone density to continuum-level bone stiffness, each element is assigned a linear isotropic behavior with parameters typically taken from micro-indentations measurements.

The big disadvantage of this approach is the need for a high-resolution CT scan, which can presently be applied only for parts of the peripheral skeleton, when scanning in situ. Another drawback is the requirement of huge computing resources, especially in the non-linear case.

1.3.3 Enhanced Continuum FE-Models

Pahr and Zysset [49] have proposed an *enhanced continuum* FE model based on high-

resolution CT images. This approach tries to combine the information and advantages of μFE and classical continuum-FE models and should be able to make better structural predictions than the classical continuum-FE model. It includes both a fabric-elasticity relationship for trabecular bone [70], which accounts for bone morphology, and anatomy-specific cortex modeling, where a smooth cortex mesh is created from the digitized cortical shell information of the high-resolution FE models [50].

This hybrid approach has the following benefits: It requires less computing resources (than a μFE model), is easily extendable to a non-linear analysis, and converges naturally to the density-only modeling for low clinical resolutions. In Ref. [49], different enhanced FE models are compared with a μFE model, taking CT-scans of 12 vertebral bodies on the basis of two different load cases (compression and shear). It was concluded that modeling a subject-specific cortical shell has an essential constraining effect on the trabecular region and therefore increases the stiffness of the whole vertebral body, which, together with modeling the anisotropy, has an essential impact on the results. Such a model provides statistically equivalent structural predictions like μFE for the two load cases but needs considerably lower computational resources (approx. 100 times faster).

The results of this approach were very promising: It has been validated experimentally on human radii [65] and on human vertebrae [14], but it has not yet been validated on human femurs.

1.3.4 Modeling of Morphology-Dependent Relationships of Human Trabecular Bone

Modeling continuum-level finite element models requires knowledge of apparent properties of bone. To describe the structure of bone on the macroscopic level, an appropriately sized Volume Element (VE) needs to be defined. If this VE is too small, a representative sampling of the microstructure is not possible. On the other hand, choosing an oversized VE results in an exaggerated averaging effect. In the following section, not only a possibility of modeling the compliance of such an appropriately-sized VE will be presented, but also the modeling of its non-elastic behavior. As an indicator of bone density, the *bone volume fraction* will be calculated (BV/TV), which is the bone volume (derived after application of a thresholding procedure), divided by total volume. In the presented equations, it will be referred to as ρ.

Elasticity

According to Hooke's law, the relation between strains and stresses of linear elastic solids can be described by the following equation:

$$\mathbf{E} = \mathbb{E}\mathbf{S} \; . \tag{1.3}$$

E and **S** are the symmetric second order tensors of strain and stress, respectively, while $\mathbb{E}$ is the symmetric, forth order compliance tensor. If one assumes orthotropy, which is one possibility to describe trabecular bone [70], the matrix form of Equation 1.3 is:

$$\begin{bmatrix} E_{11} \\ E_{22} \\ E_{33} \\ \sqrt{2}E_{23} \\ \sqrt{2}E_{31} \\ \sqrt{2}E_{12} \end{bmatrix} = \begin{bmatrix} \frac{1}{\epsilon_1} & -\frac{\nu_{21}}{\epsilon_2} & -\frac{\nu_{31}}{\epsilon_3} & 0 & 0 & 0 \\ -\frac{\nu_{12}}{\epsilon_1} & \frac{1}{\epsilon_2} & -\frac{\nu_{32}}{\epsilon_3} & 0 & 0 & 0 \\ -\frac{\nu_{13}}{\epsilon_1} & -\frac{\nu_{23}}{\epsilon_2} & \frac{1}{\epsilon_3} & 0 & 0 & 0 \\ 0 & 0 & 0 & \frac{1}{2\mu_{23}} & 0 & 0 \\ 0 & 0 & 0 & 0 & \frac{1}{2\mu_{31}} & 0 \\ 0 & 0 & 0 & 0 & 0 & \frac{1}{2\mu_{12}} \end{bmatrix} \begin{bmatrix} S_{11} \\ S_{22} \\ S_{33} \\ \sqrt{2}S_{23} \\ \sqrt{2}S_{31} \\ \sqrt{2}S_{12} \end{bmatrix} , \tag{1.4}$$

where ϵ_i are the Young's moduli, ν_{ij} are the Poisson's ratios and μ_{ij} are the shear moduli. Furthermore,

$$\frac{\nu_{ij}}{\epsilon_i} = \frac{\nu_{ji}}{\epsilon_j} \tag{1.5}$$

is given due to the symmetry property of the compliance tensor.

There are several approaches which describe the anisotropic-material behavior of cancellous bone based on volume fraction and fabric [70]. The one that will later be used in a simplified version was presented by Zysset and Curnier [71]. It assumes orthotropic symmetry and its structural anisotropy is characterized by the second-order fabric tensor:

$$\mathbf{M} := \sum_{i=1}^{3} m_i \mathbf{M}_i = \sum_{i=1}^{3} m_i \left(\mathbf{m}_i \otimes \mathbf{m}_i \right) \; , \tag{1.6}$$

$i = 1, 2, 3$ and $det(\mathbf{M}) = 1$. The eigenvectors $\mathbf{m}_i$ describe the normal directions of the orthotropic symmetry planes whereas the eigenvalues m_i reflect the extent of anisotropy. To build the fabric tensor, it is first necessary to quantify the micro-structural anisotropy (fabric) of the bone tissue. The most widely known and used method for this purpose is the mean intercept length (MIL) [11].

The compliance tensor in this approach is based on volume fraction (BV/TV) and the

positive second-order fabric tensor ($\mathbf{M}$) and is given by:

$$\begin{aligned}\mathbb{E} = \sum_{i=1}^{3} \frac{1}{\epsilon_i} \mathbf{M}_i \otimes \mathbf{M}_i - \sum_{i,j=1, i\neq j}^{3} \frac{\nu_{ij}}{\epsilon_i} \mathbf{M}_i \otimes \mathbf{M}_j \\ + \sum_{i,j=1, i\neq j}^{3} \frac{1}{2\mu_{ij}} \mathbf{M}_i \underline{\otimes} \mathbf{M}_j \ ,\end{aligned} \tag{1.7}$$

with

$$\begin{aligned}\epsilon_i &= \epsilon_0 \rho^k m_i^{2l} \ , \\ \nu_{ij} &= \nu_0 m_i^l / m_j^l \ , \\ \mu_{ij} &= \mu_0 \rho^k m_i^l / m_j^l \ ,\end{aligned} \tag{1.8}$$

where ϵ_0, ν_0, and μ_0 are material properties of the isotropic poreless bone (elastic modulus, Poisson's ratio and shear modulus), while k and l are the porosity and fabric exponents of the fabric-based elasticity relations. Although this model was designed for cancellous bone, it could theoretically also be used to describe the behavior of cortical bone, since it is hypothesized that from a micro-mechanical point of view compact bone can be considered as dense cancellous bone [6].

Plasticity and Damage

Garcia et al. [22] extended the presented model to describe plasticity and damage: Their model accounts for three distinct evolution modes: An intact elastic regime, a simultaneous flow of rate-independent plasticity and damage and a rate-independent plasticity mode.

The plastic criterion and the damage criterion were defined with the corresponding yield functions $Y^p(\mathbf{S}^p)$, which is a convex elastic domain of the stress space, and $Y^D(\mathbf{S}^D, D)$, respectively:

$$\begin{aligned}Y^p(\mathbf{S}^p, D) &:= \sqrt{\mathbf{S}^p : \mathbb{E}\mathbf{S}^p} - \sigma^p(D) \ , \\ Y^D(\mathbf{S}^D, D) &:= \sqrt{\mathbf{S}^D : \mathbb{F}^{\pm}\mathbf{S}^D} - r^D(D) \ .\end{aligned} \tag{1.9}$$

These functions are expressed in terms of the plastic stresses $\mathbf{S}^p$ and the damage stresses $\mathbf{S}^D$. $\mathbf{S}^p$ is the second Piola-Kirchhoff stress tensor and $\sigma^p(D)$ is the hardening function with the scalar $0 \leq D < 1$. The damage parameter D describes the damage accumulation of each element. The functions $\sigma^p(D)$ and $r^D(D)$ define the evolution of the radius of the plastic yield and damage criteria. This law is monotonic and describes neither the softening, the

strain rate nor densification, but the isotropic reduction in stiffness and the hardening of bone. $\mathbb{F}^{\pm}$ is the fourth-order tensor, expressed in terms of tensile (+) and compressive (-) domains, which is defined by

$$\begin{aligned}\mathbb{F}^{\pm} = \sum_{i=1}^{3} \frac{1}{\left(\sigma_{ii}^{\pm}\right)^2} \mathbf{M}_i \otimes \mathbf{M}_i - \sum_{i,j=1,i\neq j}^{3} \frac{\chi_{ij}^{\pm}}{\left(\sigma_{ii}^{\pm}\right)^2} \mathbf{M}_i \otimes \mathbf{M}_j \\ + \sum_{i,j=1,i\neq j}^{3} \frac{1}{2\tau_{ij}^2} \mathbf{M}_i \underline{\otimes} \mathbf{M}_j \ .\end{aligned} \tag{1.10}$$

Power functions were selected for the dependence of the material properties on volume fraction and fabric eigenvalues:

$$\begin{aligned}\sigma_{ii}^{\pm} &= \sigma_0^{\pm} \rho^p m_i^{2q} \ , \\ \chi_{ij}^{\pm} &= \chi_0^{\pm} m_i^{2q} / m_j^{2q} \ , \\ \tau_{ij} &= \tau_0 \rho^p m_i^q m_j^q \ ,\end{aligned} \tag{1.11}$$

where σ_0^+ and σ_0^- are the uniaxial tensile and compressive strengths, χ_0^+ and χ_0^- are the tension and compression stress interaction coefficients, τ_0 is the shear strength for a poreless ($BV/TV = 1$) bone material with at least cubic symmetry ($m_1 = m_2 = m_3 = 1$) and $i, j = 1, 2, 3$ are the indices of the principal axes.

1.4 Aim of this Work

In the course of this work it was tried to accomplish two main goals: First, a CT-imaging chamber and an experimental testing set-up were developed, which are going to be used for further studies: The CT-imaging chamber was designed for scanning femurs in an HR-pQCT machine, which is necessary to develop HR-pQCT based FE-models. After having the femurs scanned, the developed experimental testing set-up makes compression tests possible: The one-leg stance and the fall configuration can be applied to the left and to the right femur for each pair, respectively. To ensure the functionality of the designed parts and to evaluate possible improvements, three pairs of femurs were scanned and tested.

Second, a procedure to generate a nonlinear QCT based FE model was defined. For this purpose, the three pairs of femurs were also scanned in a QCT machine before testing. The resulting CT-images were then used to generate isotropic continuum-level FE models: Material properties and damage evolution were applied using a modified version of the presented model of Garcia et al. [22] in section 1.3.4.

2 Materials and Methods

2.1 Sample Selection

Three fresh-frozen matching pairs of cadaveric femurs were obtained from the clinical department of pathology, Medical University of Vienna, Austria. The medical history and descent of the donors (three females and one male aged between 63-76) is unknown. The ethical commission of the Medical University of Vienna approved this study. The bone tissue was kept frozen at -20 ° C before and in between the individual test procedure steps.

2.2 Preparation of the Specimen

The soft tissue of the proximal part of the femur was removed [9]. Special attention was paid for the cleaning of all the parts that were supposed to be embedded in the following steps. Afterwards the femur's diaphysis was cut with a handsaw approximately perpendicular to its longitudinal axis at a distance of 80 mm from the midpoint of the lesser trochanter (Figure 2.1b). The cut surface was then polished by hand with a silicon carbide paper (P500) to allow a homogeneous contact between the bone and the lower surface of the mold. This contact was meant to release the embedding as much as possible from the applied loads during the experimental test. Afterwards the bone marrow was removed from the last $\approx$ 10 mm of the medullary canal (Figure 2.1c). The resulting cavity was then closed with polymethylmethacrylate (PMMA) to seal the medullary canal and to prevent loss of fluid from the bone marrow [2].

2.3 Designing of the Tools

An important requirement was to be always able to identify the femoral position relative to the load axis. To realize this objective the femurs were embedded before starting the scanning procedure. The embedding serves two purposes: First, it constrains the bones during the

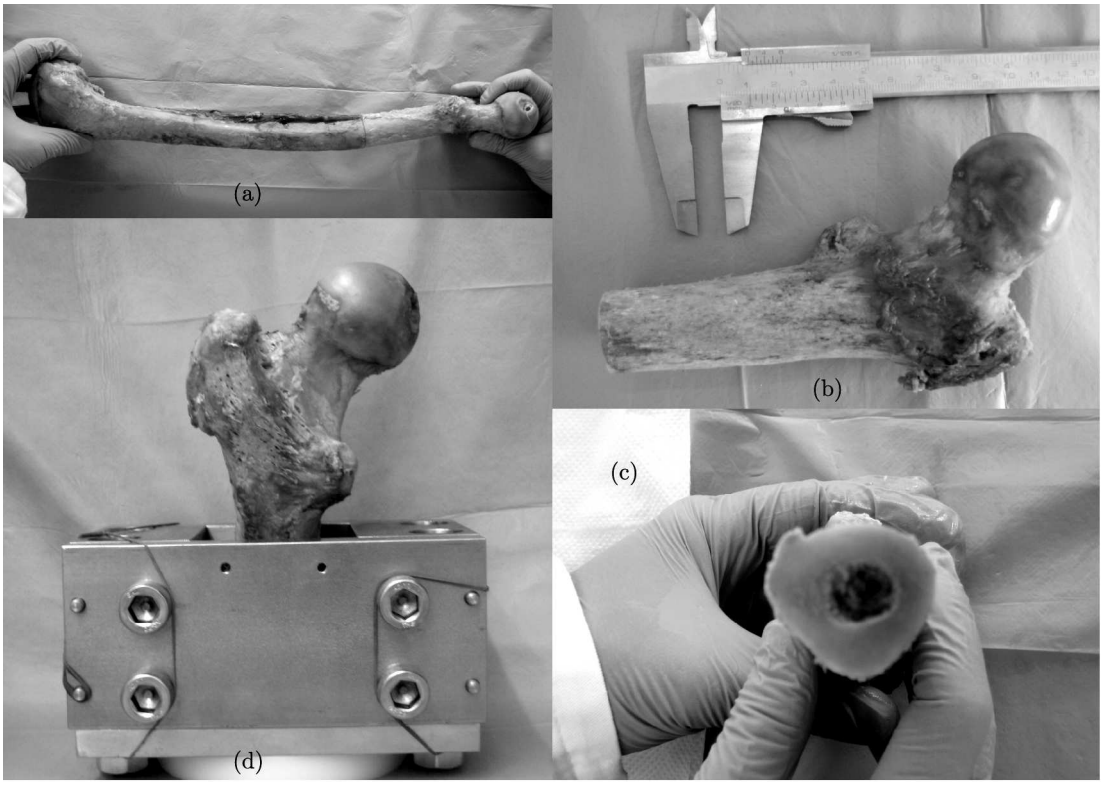

Figure 2.1: Preparation steps: (a) femur is (b) cut at a distance of 80 mm from the midpoint of the lesser trochanter; (c) bone marrow is removed from the last ≈ 10 mm of the the medullary canal; (d) the cleaned proximal femur is positioned in the mold.

experimental tests, and second, it is used as a reference to reproduce the boundary conditions of the experiments in the numerical analysis. Once the bones are embedded, it is sufficient to know the accurate position of the embedding during the experimental testing, which automatically defines the location of the femurs. This enables a meaningful comparison of numerical and experimental results.

Another goal was to design the parts for a preferably wide range of femurs, which can alter significantly in size and geometry. An overview of important femoral dimensions for the design is shown in Figure 1.2: The design is limited to the maximally allowed dimensions by an HR-pQCT (*XtremeCT, Scanco Medical AG, Switzerland*) machine. The outer diameter of the scan chamber is restricted to 120 mm, which is large enough for most femurs (and for the femurs tested so far), but could possibly fail for very large samples that have a big HAL in combination with a small neck shaft angle. The maximally possible scanning length is 145 mm, which should be sufficient for most femurs.

2.3.1 Scan Chamber

A three-dimensional drawing of the scan chamber is shown in Figure 2.2. Any parts in the field of view should not be made of metal to reduce beam hardening artifacts. Therefore, Plexiglas was used for the tube, while the other parts were made of POM-C.

"Endcap_1" can be fixed to the HR-pQCT machine, which assures that the longitudinal axis of the tube is aligned with the center line of the HR-pQCT machine. Also, the rotation of the tube inside the HR-pQCT machine is reproducible. For the QCT (*Brilliance64, Philips, Germany*) scan, only rough alignment is possible: There the cylinder is placed on the bed without any exactly defined fixation. "Endcap_2" only closes the cylinder and does not serve as a reference. All other parts are screwed on "Endcap_1" using nylon setscrews, which also take care of the proper alignment of the other parts. The "Holder" is used to clamp the embedding block, which is molded with the construction presented in section 2.3.2 (the mold's inner shape is a prism with a trapezoidal cross-section). The "Holder" consists of two parts that can be screwed together to grip the parallel surfaces of the embedding block. This way it is possible to move and rotate the embedding in the plane parallel to the not-inclined sides.

The maximal length of the femur that can be scanned is given by the scanning window and amounts to 145 mm. Including the embedded shaft, most femurs would be bigger. Therefore, the length of the Plexiglas tube was chosen larger than the scanning window (200 mm), which results in an only partly scanned femoral shaft: 12 mm are scanned, which is necessary, since the embedding is used as a reference system.

If the femur is shorter, "Distance discs" can be used: They are placed between "Endcap_1" and the "Holder" to be able to scan as much of the femur as possible, given that smaller femurs can be moved to the end of the tube. This is important for the later numerical analysis, which is improved by the possibility of modeling the embedding of the femoral shaft.

The prism-like phantom (Figure 2.2b) is too large to be placed together with the femur in one cylinder. Therefore, an additional chamber is needed in order to scan the phantom (Figure 2.2b) in the HR-pQCT machine. The design of this chamber is similar to the one already presented. The phantom is arranged between a slightly changed "Endcap_1" and a "Distance disc", which is placed next to "Endcap_2" and serves to avoid axial movement of the phantom. Now, the modified "Endcap_1" has three additional small pins attached by a tight fit to the inner side of the endcap, which fix the phantom against rotation by means of the small pins.

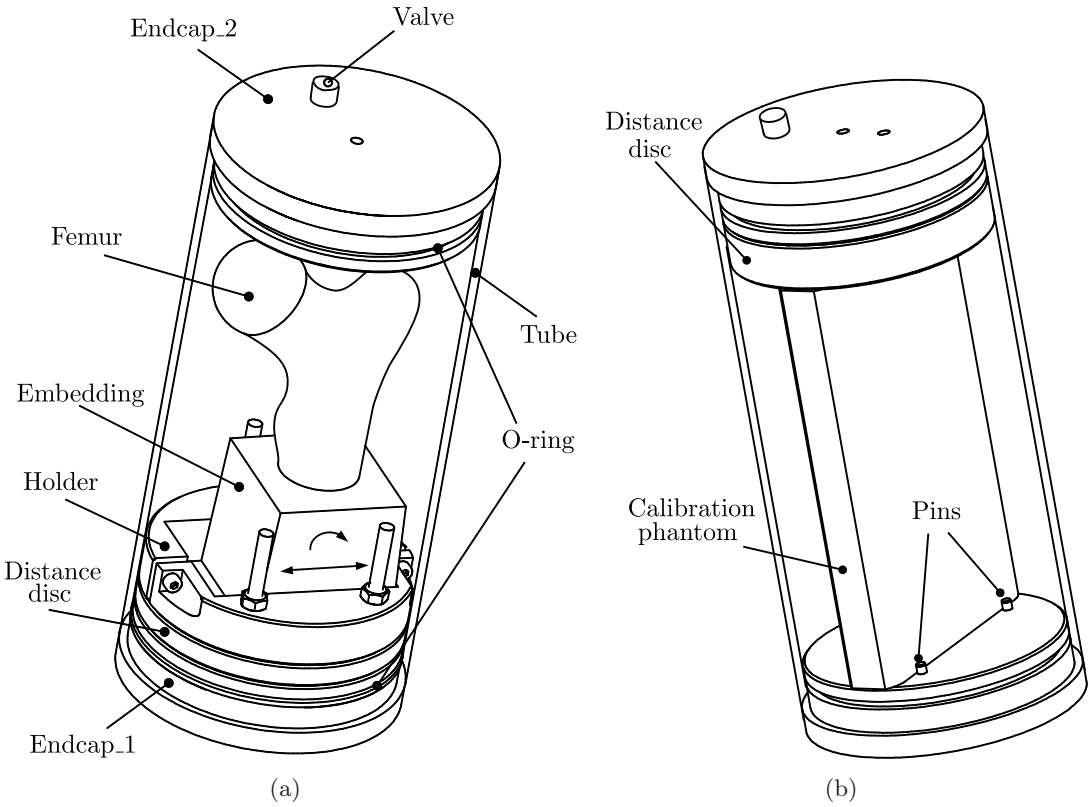

Figure 2.2: Isometric view of the HR-pQCT chamber. The arrows describe the possible translation and rotation of the embedding. (a) shows the configuration for scanning the femurs, (b) shows the configuration for scanning the calibration phantom.

Since the chambers are filled with liquid during the scanning procedure, o-rings and valves are attached to the ”Endcaps“.

2.3.2 Experimental Testing Setup

There are many possible stance- and fall-loading conditions; some were already mentioned in the introduction. It was decided to apply load configurations similar to those used by Ref. [32]. The right femurs were used to simulate impact from a fall to the side (fall configuration), the left femurs should simulate spontaneous fractures (one-leg stance configuration). These configurations were chosen, because they were shown to produce clinically relevant fractures [32].

In the fall configuration, opposing forces were applied to the femoral head and the greater trochanter at 60° to the shaft and the femur was internally rotated by 20° (Figure 2.3). The greater trochanter was put in contact with a custom-molded PMMA cup that rested on a

surface opposite the loading platen. In the stance-like configuration, force was applied to the femoral head at 20° to the shaft axis in the plane that is defined by the neck axis and the shaft axis.

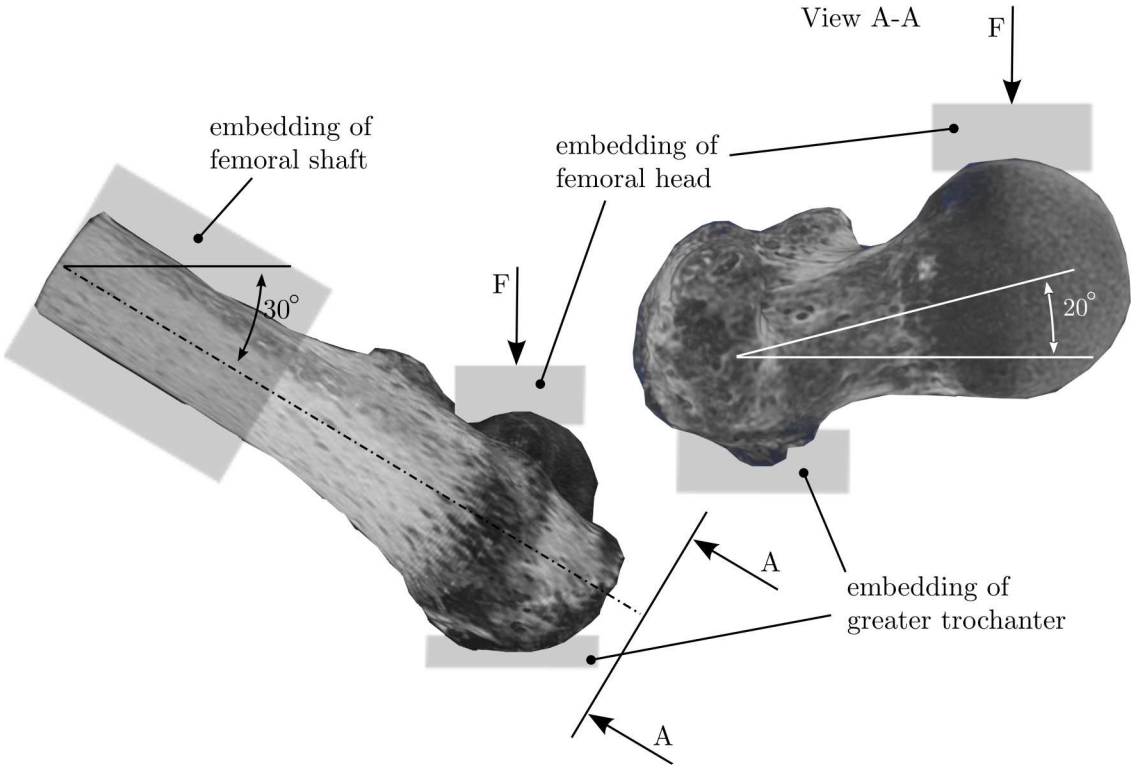

Figure 2.3: Descripion of the tested femoral position in the fall configuration.

In the stance load configurations, the upper 6 mm, in the fall configuration, the upper 3 mm of the femoral head were embedded in PMMA to achieve a distributed loading. A compression test of a tryout specimen showed the importance of embedding the femoral head to avoid a non-relevant type of failure of the femoral head. Figure 2.4 shows the induced fracture resulting from loading with a plane surface without embedding the femoral head.

The shaft was restrained by embedding it in PMMA. The inclination between shaft axis and load axis was taken care of by the "inclined blocks" (section 2.3.2). The second rotation needed to be fixed within the embedding procedure by positioning the femur correctly in the mold.

For the design of the experimental testing setup, it was important to estimate the maximal loads that were applied during the mechanical tests. Therefore, some literature research was done to estimate the maximal loads that would be supported by the femurs. A small

Figure 2.4: Non-clinical-relevant fracture, which was produced in a compression test without embedding the femoral head.

Table 2.1: Maximum failure loads of different research groups.

Authors	Load configuration	Maximum failure load	Displacement rate
Keyak et al. [35]	Stance	15 kN	0.5 mm/s
	Fall	4.6 kN	0.5 mm/s
Cody et al. [9]	Stance	16 kN	0.21 mm/s
Cheng et al. [7]	Fall	9 kN	14 mm/s

representative selection of published results is presented in Table 2.1. The stance load configuration is expected to support much higher forces (up to 16 kN) than the fall configuration (up to 9 kN). Furthermore, it includes a bending moment that is highly dependent on the geometry of the tested femur. Considering the maximal force which the machine can apply (15 kN) (this is a little smaller than the highest load measured by Cheng et al. [7]), and the geometry of the femurs (Table 1.2), one can roughly estimate the highest possible bending moment with

$$M = F * a = F\,[\mathrm{FHO}\cos(20) - (80 + b)\sin(20)] \approx 375\,\mathrm{Nm},$$

where FHO and b are estimated as 63 mm (Table 1.2) and 20 mm (Figure 2.5) respectively. As this load moment in conjunction with the axial force might damage the pre-installed load cell (15 kN), which is placed at the bottom of the frame of the MTS machine. Therefore, a 100 kN load cell (*U3 force transducer, HBM, Germany*), which was placed above the loading platen, was used to measure the load during the experiments.

We decided to choose stainless steel as a material for the parts having contact with biological tissue (part 1-"mold" and the loading platen) for two reasons: The first reason was to

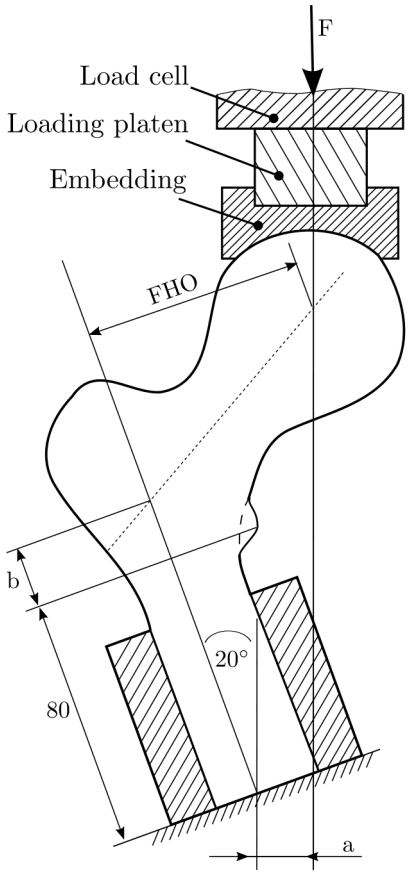

Figure 2.5: Estimation of the bending moment

avoid corrosion since these parts would constantly be in contact with saline solution, which would be used to keep the femurs wet. Second, we looked for a material with a negligible deformation under the expected high loads. The other parts are made of steel to account for the loads and are tried to be kept dry during the experimental tests.

The experimental testing setup (Figure 2.6) can be divided into four main parts:

- Part 1 (connection), connects the construction with the testing machine;
- Part 2 (mold), actually holds the embedding of the femur and is also used as a mold;
- Part 3 (inclined blocks), are responsible for the right inclination;
- Part 4 (positioning plates), is used for an exact plane positioning in order to place the femoral head right under the load, since the loading machine only allows for vertical movement.

As mentioned earlier in this section, the experimental testing setup needs to be capable of loading the femurs in two different load cases: The one-legged stance and the fall configu-

ration. This was handled by using two different inclined blocks (part 3). Part 2 (mold) is screwed on one of these blocks, depending on the load case.

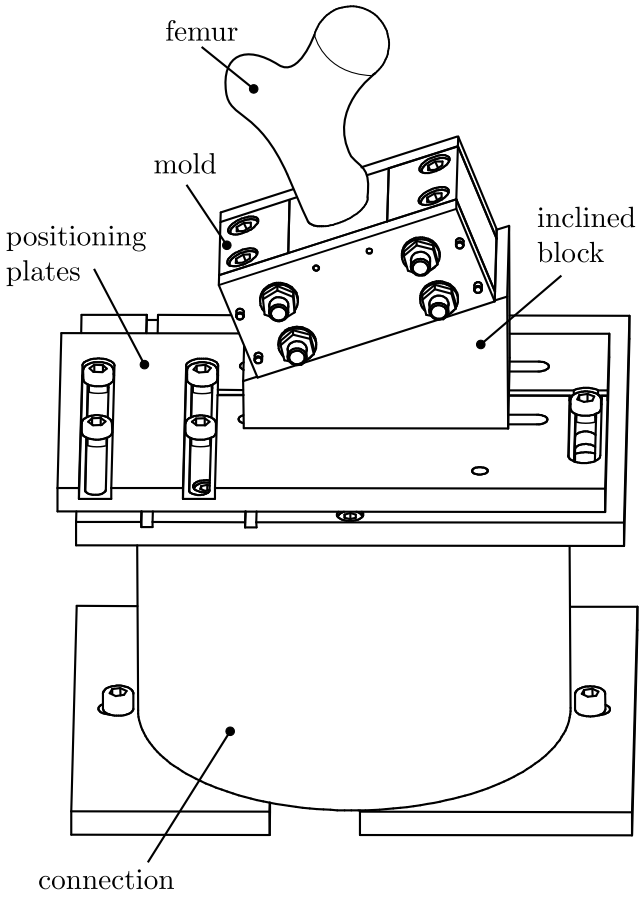

Figure 2.6: Isometric view of the testing setup (stance configuration)

Part 1 - Connection

The testing machine is also used for other projects, which normally use a 15 kN load cell, which is placed at the bottom of the construction, directly on the frame of the testing machine. However, since high loads, consisting of axial loads plus a bending moment, are expected, we decided to use the external load cell, which can support loads up to 100 kN. To protect the MTS load cell, a frame, which was directly screwed to the frame of the testing machine, was wrapped around the load cell. All other parts are connected to this unit. This way the MTS load cell is protected and it is easy to switch from one test setup to the other.

Part 2 - Mold

This part is used to fix the femoral shaft during the test, and is also used as a mold. Therefore, easy removal of the embedding was an important goal. This was accomplished by making the mold out of two plates and two blocks, connected by screws (Figure 2.7). These parts can easily be removed from each other. Moreover, smooth surfaces were demanded (roughness Ra $< 3.2\,\mu$m) to prevent the embedding from sticking to the mold. For a proper alignment, reference pins were used, two for each connection. These pins can be removed before untacking the mold. Two inner sides of the assembled part are inclined (3°). This way, the embedding block is fixed against translation (because of the two inclined sides) and rotation (because of its rectangular shape).

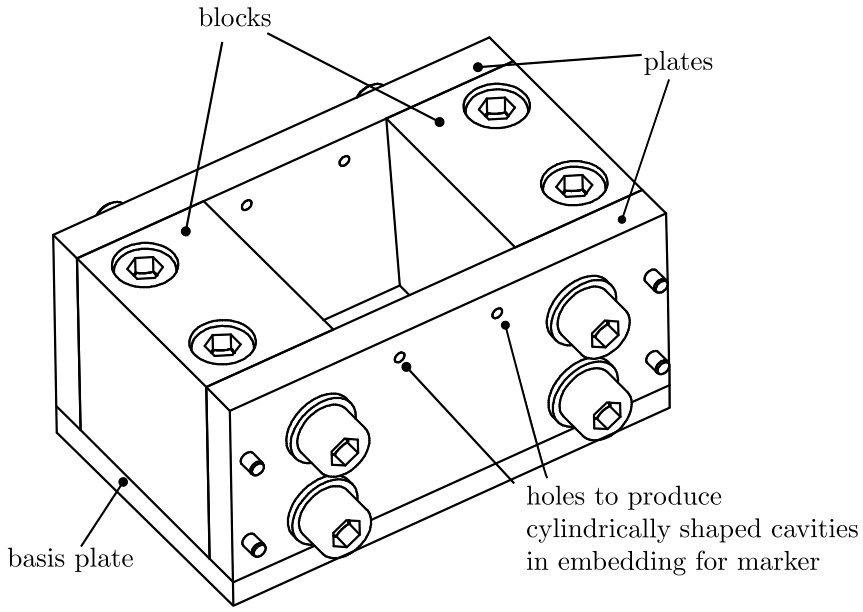

Figure 2.7: Isometric view of the mold

Part 3 - Inclined Blocks

As mentioned at the beginning of this section, we decided to orientate ourselves to the setup of Keyak et al. (e.g. [35]). According to this setup, the shaft of the tested femur needs to be positioned 30° (fall configuration) or 70° (stance configuration) to the horizontal plane. Therefore two massive blocks with inclination angles of 20° and 30° to the horizontal plane are used, whose only purpose is to adjust the angle of inclination of the femoral shaft correctly.

The mold is screwed to the inclined block, which in turn is screwed on the positioning plates (see next paragraph). The exact alignment between the positioning plate, the inclined block and the mold is ensured again through pins and a demanded roughness Ra $< 3.2\,\mu$m.

When assembling the testing setup, the inclined blocks need to be bolted down, which can only be done, when the two positioning plates are separated. The usage of flanges would make this procedure unnecessary, but would also increase the needed size and weight of the construction considerably.

Part 4 - Positioning Plates

The mold that grabs the embedded femur and which is screwed to one of the inclined blocks needs to be positioned in the plane perpendicularly to the load direction. Since the position of the femur always needs to be exactly defined, this movement is realized by two plates ("positioning plate 1 and 2"), each is responsible for one direction (Figure 2.8). The two planes of these plates are parallel ($\| < 0.05\,$mm) and have a roughness Ra $< 3.2\,\mu$m.

Each moving part (inclined block and plate 2) has two pins extending the plane surface, which move in a slot of the other part, allowing translation in only one direction. Positioning plate 1 is fixed to the connection part and serves as a reference, since its middle is aligned with the load axis of the machine. The inclined block is fixed to positioning plate 2 with four screws. Positioning plate 1 has two slots to account for the two load configurations. This makes it possible to use the same plates for both load cases.

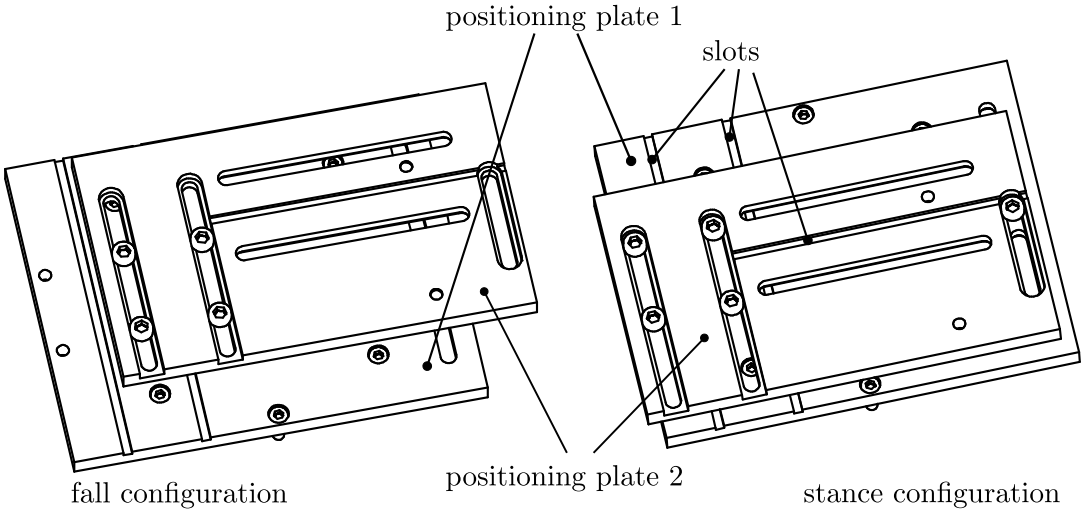

Figure 2.8: Isometric view of the positioning plates: The left image shows the fall configuration, the right image shows the stance configuration.

2.4 Embedding Procedure

59 mm of the most distal part of the femoral diaphyses were embedded in PMMA, using the construction presented in section 2.3.2 as a mold. For this task, the femur was positioned in the mold (Figure 2.1d) with consideration of the selected load case, see section 2.3.2. The neck axis was estimated and sketched with a marker on the surface of the femurs. The femurs were positioned such as this mark was either parallel (stance configuration) or 20° (fall configuration) to the plates of the mold (Figure 2.7).

The femoral head was covered with plasticine to produce a flat surface, on which a weight of 1.25 kg could be placed. As a result of the weight and the polished surface of the femur's diaphysis the femur was firmly standing on the bottom of the mold ("basis plate" in Figure 2.7). It proved to be important to polish all inner surfaces of the mold, which were going to be in contact with the embedding material, with a release spray. This made the disassembly after testing easier.

One more task should be mentioned: The used embedding material is not shown in the HR-pQCT-scans. However, its exact position needs to be known for correct generation of the FE-models. Therefore, four greased additional pins were placed in the mold to leave four cylindrically shaped cavities in the embedding, which helped later to identify the exact position of the embedding.

Finally, the liquid embedding material (PMMA) was poured into the mold, taking around 15 minutes to harden. The embedding material heated up to approximately 40° to 50° C, which leaded to a separation of liquid bone marrow. As a result, the femoral shaft was partly covered by a greasy coating, which was later identified by means of the QCT-images.

After the hardening process, all pins were removed and the mold was untacked. The four cylindrically shaped cavities in the embedding (left from the additional pins) were then filled with cement that is shown in the CT-images.

As mentioned in section 2.3.2, parts of the femoral head and of the greater trochanter were embedded to distribute the force during the test. In particular, they were embedded within the testing procedure, after positioning the femur on the mounting jig. An aluminum cylinder with a diameter of approximately 53 mm and a wall thickness of approximately 0.1 mm was placed atop the femoral head, covering the top 6 mm. Every gap was closed with plasticine (Figure 2.9). The distance between loading surface and femoral head was adjusted to 10 mm. Then PMMA was poured into the cylinder, covering parts of the femoral head (6 or 3 mm, in stance and fall configurations, respectively) and parts of the loading platen (approximately

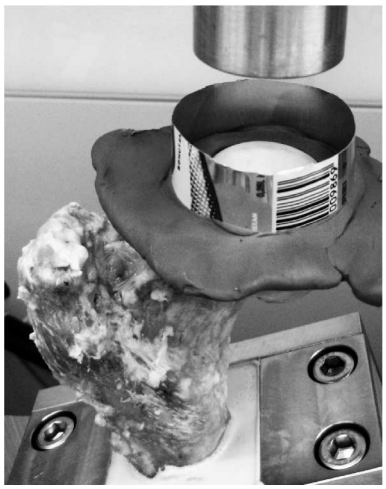

Figure 2.9: Preparing the mold for embedding the femoral head: Before starting the embedding, the loading platen will be lowered to a distance of 10 mm to the femoral head.

10 mm). The loading platen was partly embedded to avoid translation and rotation of the embedding material in respect to the loading platen during the test. After the embedding process, the aluminum cylinder was removed. To embed the greater trochanter, a mold was formed with plasticine, high enough to embed 3 mm of the greater trochanter. To avoid the embedding to stick to the translation guides, an aluminum plate with a thickness of 3 mm was screwed on the positioning plate.

2.4.1 Embedding Material

Choosing the right embedding material is a difficult task, since it needs to fulfill different requirements:

- High Stiffness compared with the femurs: The embedding material should have a high Young's modulus.
- Easy Handling: It should be easy and relatively fast to mold.
- Low shrinking during the hardening process
- Low Hardening Temperature: The temperature should stay below $\approx 50°$, since the bone should not be damaged.
- The embedding's radio-opacity should differ from the bone's radio-opacity. The embedding material should be displayed in a distinct color in the CT-scans.

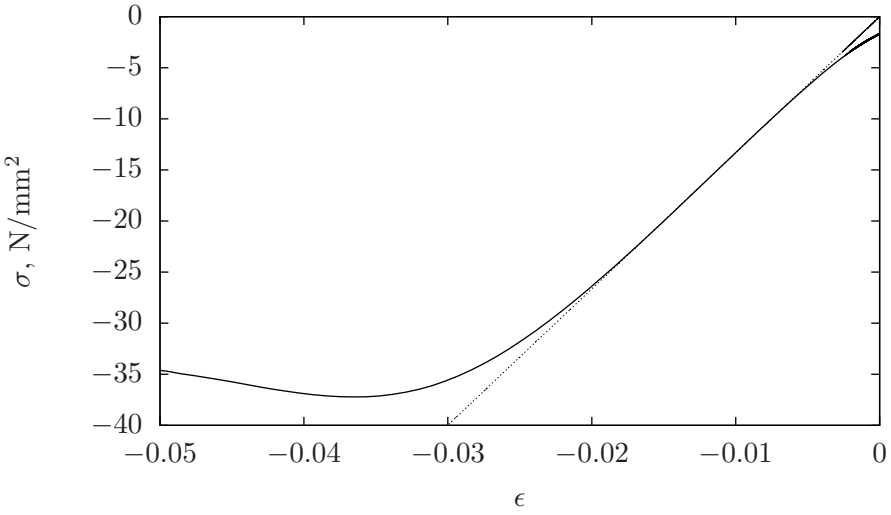

Figure 2.10: Typical stress-strain curve of the embedding material (PMMA), taken with a compression test.

PMMA was chosen as an embedding material: Its hardening temperature is approximately 40° to 50° C, almost no shrinking occurs and it is very easy to handle. However, these advantages are achieved at the expense of a relatively low stiffness (E ≈ 1.3 GPa), which was measured by running a compression test as following: Ten cylindrically shaped specimen of embedding material with the diameter $d \approx 8$ mm were molded. After hardening they were cut and polished to the length of $l \approx 12$ mm. Then a stress-strain curve was measured by applying a displacement-controlled axial force with a servohydraulic testing machine (*Mini-Bionix, MTS system, U.S.A.*). Figure 2.10 shows a typical stress-strain curve that is representing the results. Table 2.2 shows the mean values and standard deviations of the calculated properties of the embedding material.

Table 2.2: Material Properties of the Embedding Material (PMMA) (mean value ± standard deviation).

Young's Modulus	1263.5 ± 53.5 MPa
Ultimate Strength	-35.3 ± 1.6 MPa
Ultimate Strain	-0.037 ± 0.001

2.5 In vitro Experiments

The testing setup is composed of a mounting jig, loading and measurement equipment and data acquisition equipment. The mounting jig and the applied constraints were already presented in section 2.3.2.

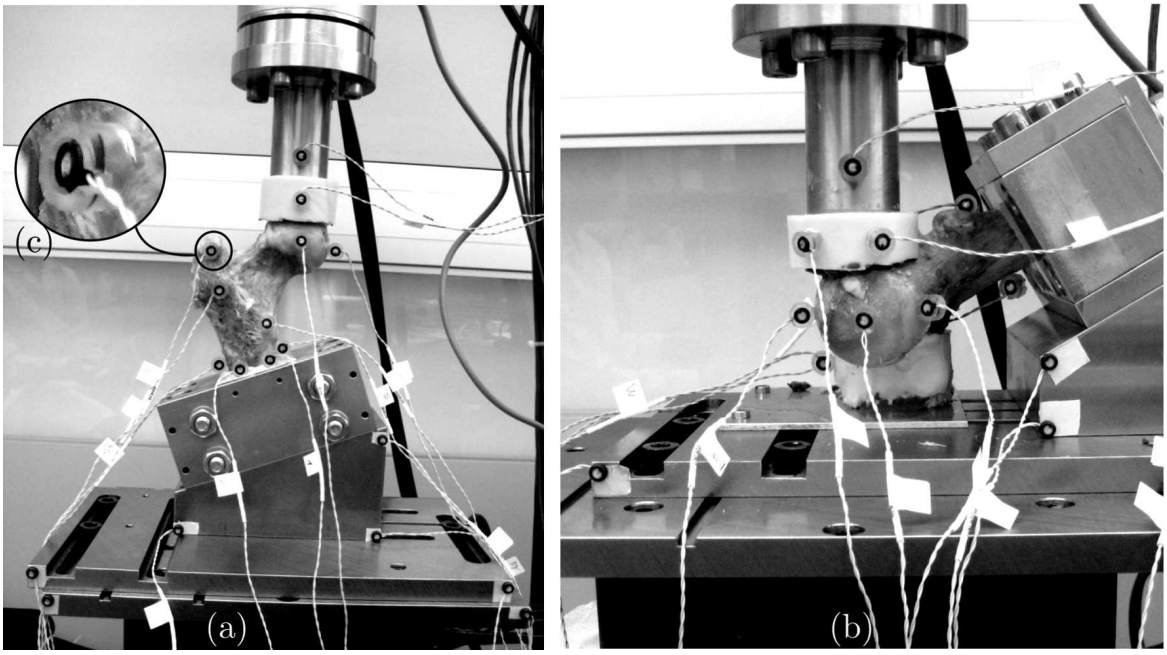

Figure 2.11: Proximal femur in the stance (a) and fall (b) loading conditions. In the fall configuration, opposing forces were applied to the femoral head and the greater trochanter at 60° to the shaft and 70° to the major axis of the elliptical cross-section of the neck ("neck axis"). For the stance configuration, force was applied at 20° to the shaft, which was restrained in both configurations. Markers are placed in plastic rings and fixed with gluten to the femur (c).

The femurs were thawed and then submerged in 0.9 % saline solution for at least one hour before testing and were kept wet until experimental testing. The bones were loaded by the displacement-controlled servo-hydraulic testing machine with a preload of approximately 100 N. Then a linear compression ramp which simulated quasistatic loading was applied with a displacement rate of 5 mm/min until femur failure.

The axial force was measured by means of the 100kN load cell, which was placed above the loading platen. Additionally, a motion-capture system (*Optotrak Certus, Northern Digital Inc., Canada*), which is capable of measuring three dimensional movements with a resolution of 10 μm was used. Up to 20 markers (dependent on the geometry and load configuration) were placed on different locations of the testing setup and the femur to examine local displacements (Figure 2.11). Markers were placed on the mounting jig (translation plates and inclined block) to (1) estimate its compliance and to (2) define a new coordinate system for the motion-capture system. The three markers on the inclined block represented two axes of the new coordinate system, the third axis was defined orthogonal to these axes (Figure 2.12). The such defined coordinate system was aligned with the load axis and made it easier to interpret the data of the different data acquisition systems.

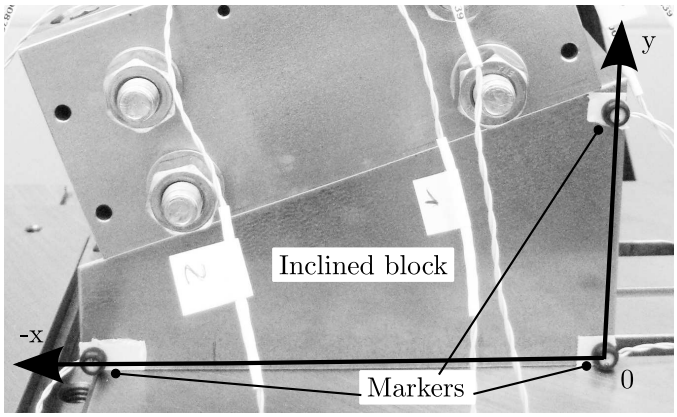

Figure 2.12: Three markers on the inclined block define two axis of the coordinate system of the motion-capture system.

In addition, some markers were placed on the embeddings (embedding of femoral head, greater trochanter and shaft) to analyze their compliance. The remaining markers were placed on the loading platen (one marker) and the femur itself: Points of interest were the lesser (one marker) and greater (up to three markers) trochanter, the femoral head (up to three markers) and the shaft (two markers), as near as possible to the embedding. To position the markers on the femurs, they were placed in plastic rings, which were glued to the bone. The markers, that measured the displacements of the metal parts (loading platen, inclined block, etc.), were fixed with a double-faced adhesive tape.

The data acquisition was achieved by 50 Hz (load cell) and 100 Hz (motion-capture system and MTS), respectively. The motion-capture system was started some seconds before applying the load. The captured values were used to evaluate the accuracy of this system. Additionally, the experiments were captured with a video camera.

2.6 Scanning Procedure

Each femur was scanned in the QCT and the HR-pQCT machine go get a 3D-map of the BMD distribution. In both cases, the custom-made Plexiglas chamber (see section 2.3.1) was used to position the femurs properly. For converting Hounsfield Units (HU) to equivalent ρ_{QCT} in mgHA/cm^3 a Bone Density Calibration Phantom (BDC Phantom, QRM GmbH, Germany) was used, which contained three certified hydroxyapatite solution inserts. These inserts consisted of different amounts of Epoxy resin, $CaCO_3$ and HA powder ($Ca_5(PO_4)_3OH$) and CTWater®, respectively, having a defined partial density of pure HA ($0, 102.2$ and $204\,\mathrm{mgHA/cm^3}$).

The images of the HR-pQCT- scans will be used for calculations in future works, while the QCT- scans were used for the FE model generation in this paper.

2.6.1 QCT - Scanning Procedure

The femurs where placed in the water-filled Plexiglas chamber (see section 2.3.1) to reduce streak artifacts due to material interfaces and to simulate soft tissues around the femur [4]. Then the chamber was placed atop the calibration phantom. Afterwards the phantom and the chamber were placed on the bed of the QCT machine. It was tried to align the axis of the chamber with the axis of the QCT scanning machine as well as possible. Subsequently a CT scan of the femur and the phantom was taken with the QCT machine (120 kVp, 200 mA, contiguous 1.0 mm-thick slices,). The isotropic in plane pixel size differed, depending on the femur (0.215 mm and 0.195 mm pixels).

2.6.2 HR-pQCT- Scanning Procedure

The scanning time took approximately one hour per femur. Including travel time etc., the femurs were submerged in liquid for approximately six hours. Therefore, the Plexiglas chamber was filled with an 0.9% NaCl saline solution to prevent the femurs from losing mineral. Then the chamber was attached to the HR-pQCT machine by using screws, which ensured proper and well-defined alignment. The Plexiglas cylinder containing the phantom was always scanned first, followed by two cylinders, each containing one femur (60 kVp, 1 mA, contiguous 0.082 mm-thick slices, 0.082 mm pixels). This way, a scan of the phantom was used to calibrate two femurs.

2.7 Calibration Procedure

The calibration from Hounsfield Units to ρ_{QCT} was done similarly to the procedure described in [60]. Three volume with quadratic cross-sections of $10 \times 10\,\mathrm{mm}^2$ and a height of approximately 4/5 of the phantom length's were cropped from each scanned image. Each region consisted completely of the volume of a rod, having a given partial density of pure HA. Then the mean gray values of the cropped voxels were calculated. Afterwards, a linear regression between gray values (Hounsfield Units) and equivalent ρ_{QCT} was achieved with the assumption that the relationship Hounsfield Units - ρ_{QCT} remained linear beyond the density range of the phantom ($0 - 200\,\mathrm{mgHA/cm}^3$) [41]. This way, one calibration function

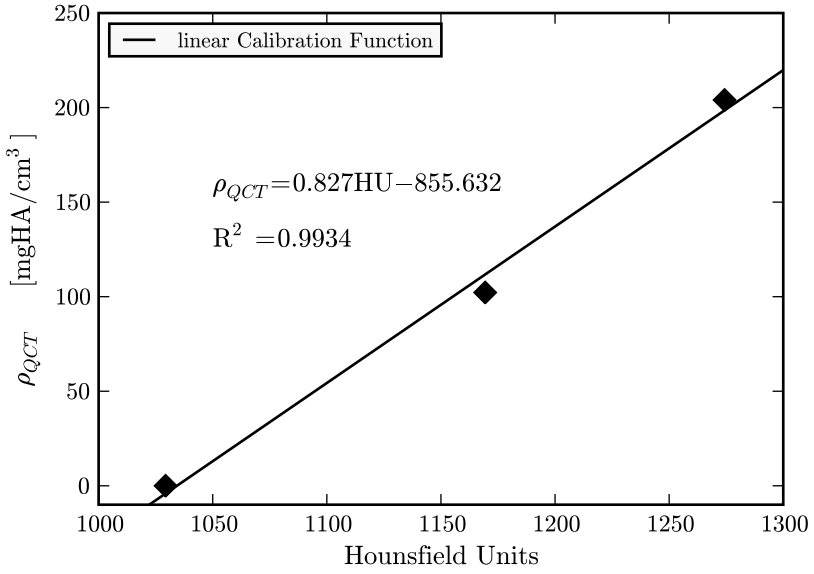

Figure 2.13: Calibration Curve: ρ_{QCT} and corresponding HU

was calculated for every scan, equation 2.1 shows one example, which is also shown in Figure 2.13:

$$\rho_{QCT} = 0.8273 \text{ HU } - 855.63 \,, \tag{2.1}$$

where ρ_{QCT} is expressed in mgHA/cm^3. It was also checked if it was necessary to adjust the resulting calibration function over the scanning length by dividing a scan of one phantom into five equally sized cuts and calculating one calibration function for each section. However, the measured gray values hardly changed over the measured length, the maximal difference was $\approx 1\%$.

Concerning the calibration of the QCT-data, the cropping had to be done manually, since the position of the phantom relatively to the Plexiglas chamber and to the scanning machine varied each time and did not allow to apply the same mask to every scan. Calibrating the scans of the HR-pQCT was not done in this work, but it could be done in an automatic manner, since the construction of the scan chamber ensures a fixed position of the phantom in the HR-pQCT machine.

As a next step a calibration function must be defined to assign a BV/TV value to each voxel. Different ρ_{QCT}-BV/TV relations have been used by diverse research groups: Dall'Ara et al. [14] used a linear relationship assuming 0 % BV/TV at 0 mgHA/cm^3 and 100 % BV/TV at 1059 mgHA/cm^3. Perilli et al. [52] concluded the following relation between ash density

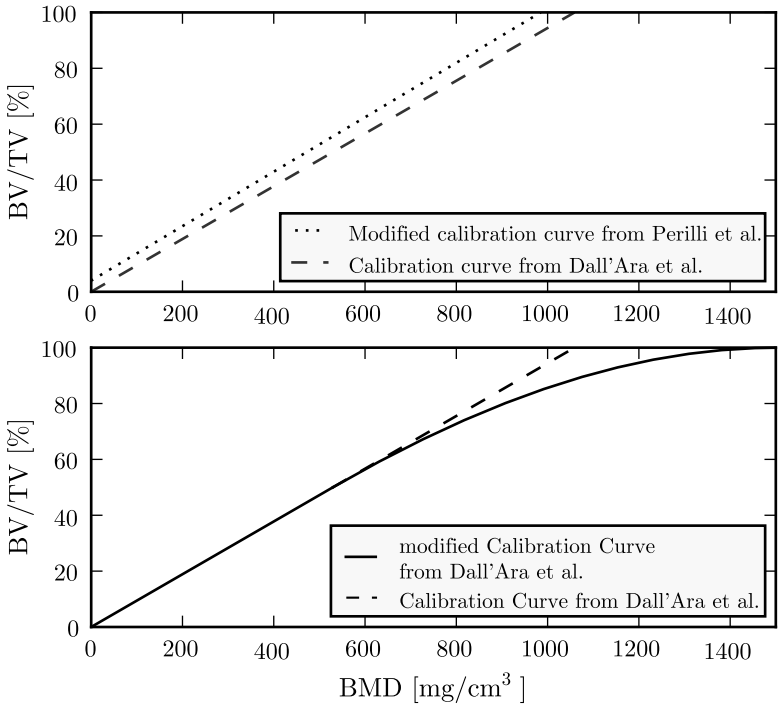

Figure 2.14: Calibration curves: ρ_{QCT}-BV/TV relations of Dall'Ara et al. [14], Perilli et al. [52] (modified by using the $\rho_{ash} - \rho_{QCT}$ relationship of Schileo et al. [60]) and modified calibration curve of Dall'Ara et al. [14] that was used in this work.

(ρ_{ash}) and BV/TV:

$$\rho_{ash}\ [\mathrm{g/cm^3}] = 0.009 * \ BV/TV + 0.043\,\mathrm{g/cm^3}.$$

With the assistance of the following $\rho_{ash} - \rho_{QCT}$ relationship

$$\rho_{QCT}\ [\mathrm{gHA/cm^3}] = -0.09 + 1.14\rho_{ash}\ [\mathrm{g/cm^3}], \tag{2.2}$$

published by Schileo et al. [60], Perilli et al. assumed a BV/TV of 100 % at 985 mgHA/cm^3. The presented relationships are very similar and are shown in Figure 2.14. Both equations were extracted from data of trabecular bone, a linear relationship beyond the trabecular bone's density range was assumed. Varga and Zysset [64], on the other hand, assumed 1200 mgHA/cm^3 to be the density of fully mineralized tissue.

However, by taking a look at the ρ_{QCT}-scaled QCT images, much greater values were noticed. Figure 2.15 shows a representative distribution of ρ_{QCT} values, taken from one QCT image ($0.215 \times 0.215 \times 1\,\mathrm{mm^3}$). As one can see, the distribution of ρ_{QCT} shows a peak slightly below 1400 mgHA/cm^3, which represents the cortical shell. The question comes up if this is

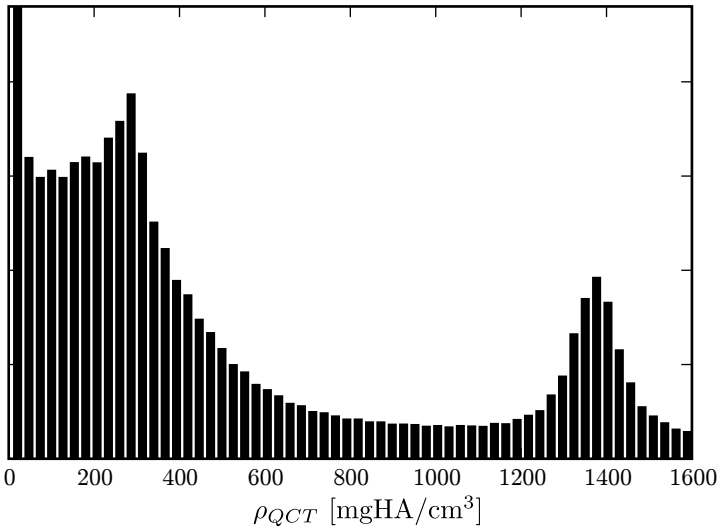

Figure 2.15: Representative histogram, taken from a ρ_{QCT} scaled QCT image ($0.215 \times 0.215 \times 1\,\mathrm{mm}^3$)

a realistic value, or if the assumption of linear behavior of the relation ρ_{QCT}-HU is wrong. Amongst others, Schileo et al. [60] investigated the relationship of ρ_{QCT} to ash density by taking cortical and trabecular samples of human and bovine bone (Equation 2.2). In the course of this work, they measured ash densities, that correspond to ρ_{QCT}-values up to approximately $1450\,\mathrm{mgHA/cm}^3$, which is about the value of the peak in Figure 2.15.

Hence, defining the density of fully mineralized tissue and the calibration curve to calculate the BV/TV of proximal femurs is an unresolved problem, which should be investigated more closely. Here it was concluded that the calibration curve of Dall'Ara et al. [14] (Figure 2.15) can be used in the range between 0 and 50% BV/TV, since this range has been proven experimentally. The other part of the calibration curve was adjusted to fit the calculated ρ_{QCT} and is unfortunately not validated: A value of $1500\,\mathrm{mgHA/cm}^3$ was assumed to match 100% BV/TV, a slope of 0 was defined for 100% BV/TV and the resulting calibration curve should be continuously differentiable. Finally, a cubic spline with the given boundary conditions was calculated to connect 50% and 100% BV/TV (Figure 2.14), which results in the following equation:

$$\begin{aligned} BV/TV = 50 + 0.0944 \cdot (\rho_{QCT} - 530) - 3.5427 * 10^{-5} \cdot (\rho_{QCT} - 530)^2 \\ -9.1049 \cdot 10^{-9} \cdot (\rho_{QCT} - 530)^3 \,, \end{aligned} \tag{2.3}$$

where BV/TV is expressed in % and ρ_{QCT} is expressed in $\mathrm{mgHA/cm}^3$.

2.8 Finite element modeling

2.8.1 Voxel-based Mesh Generation

For most steps of the mesh generation, a previously developed in-house script (*"mic.py"*) from the medtool framework was used. This script is a converter/filter for medical CT image files (voxel models). Furthermore, the usage of this script allows the conversion of every single voxel directly into an 8-node brick element, except voxels with a value of 0, which are not exported. In addition, it is able to export all border nodes and elements of the generated mesh in specific sets that can be used to define the boundary conditions. To make FE-model generation as easy and automatic as possible, adjusting the models in a graphical preprocessing software was avoided, every manipulation was voxel-based and done by the *"mic.py"*-script.

After the scanning procedure, the QCT images were slightly misaligned. The plane surfaces of the embedding blocks, which were normal to the shaft axis, were not parallel to the scanning slices. These misalignments needed to be corrected manually by taking the cement markers of the embedding (see section 2.4) as a reference and measuring the inclination angle. Additionally, it was necessary for the load axis to be either perpendicular or parallel to the image slices, due to modeling issues. The rotations were done by applying ITK (*Insight Segmentation and Registration Toolkit*) transformation filters (ResampleImageFilter) to each QCT data set. The subsequent steps were taken using the *"mic.py"*-script.

The calibration functions discussed in section 2.7, were applied to convert the HU to ρ_{QCT} values first and afterwards to BV/TV values. Then the slices were resampled with a factor of five to $0.975 \times 0.975 \times 1\,\mathrm{mm}^3$ and $1.075 \times 1.075 \times 1\,\mathrm{mm}^3$, respectively, to reduce computational time. In addition, the images were also resampled with a factor of 10 and 15 to investigate the convergence behavior of the images. Before resampling was done, voxel rows were added to the images. As a result, the dimensions of the images were multiple of the resolution factors, which should minimize averaging effects. After resampling, the images were segmented to define the outer contours of the femurs. Segmentation was done by using the *"Fill + Closing"* algorithm, presented in [50]. The global threshold was chosen differently for the different resolutions. 16% BV/TV was chosen for the 1 mm resolution, 13% BV/TV was chosen for the 2 and 3 mm resolutions. The thresholds were chosen visually and seemed to be the best choice for masking the femurs. Having done the segmentation and resampling, the BV/TV-values were scaled to a range of 1-250, meaning that a BV/TV-value of 0 corresponds to a gray value of 0, and a BV/TV-value of 1 corresponds to a gray value of 250, resulting in 250 different material cards.

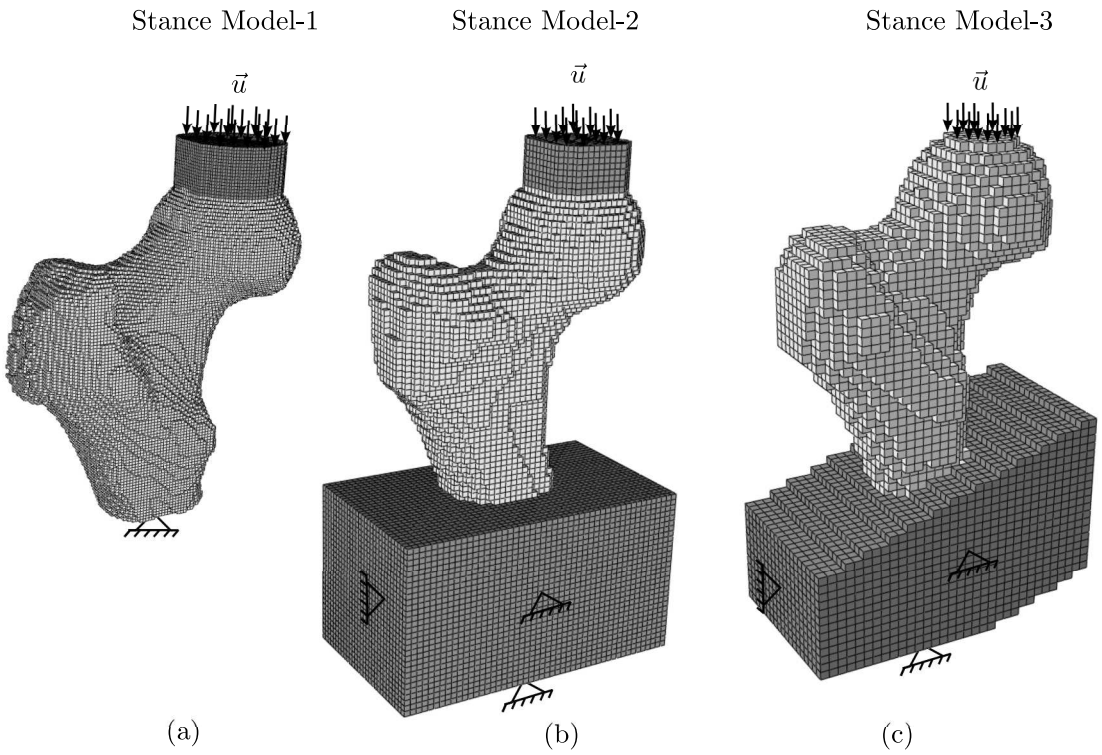

Figure 2.16: Examples of a 1 mm (a), a 2 mm (b) and a 3 mm (c) mesh to simulate the stance configuration.
(a) Model-1, where the femoral shaft is cut off at the beginning of the embedding, the nodes of the resulting surface are fully constrained.
(b) Model-2, where the femoral shaft is embedded. The embedding is enlarged towards the borders of the image for easier exporting its border nodes as node sets, which are fully constrained.
(c) Model-3, where the femoral shaft is embedded. The embedding is perpendicular to the shaft-axis, and its borders are enlarged towards the borders of the image for easier exporting its border nodes as node sets, which are fully constrained.

To simulate the embedding material, voxels with a gray value value of 255 were added. This gray value is above the range of the gray values that correspond to the BV/TV-values. Therefore, voxels having this gray value can afterwards be assigned a proper and distinct material property. Three different models were created to investigate the influence of changing boundary conditions. In Model-1 (Figures 2.16a and 2.17a), the femoral shaft was cut off approximately at the beginning of the embedding material, perpendicular to the load axis. In Model-2 (Figures 2.16b and 2.17b), the embedding material of the shaft was also modeled, with surfaces parallel and perpendicular to the load axis. Model-3 (Figure 2.16c) was similar to Model-2, except the embedding material was rotated to be perpendicular to the femoral shaft axis.

The femoral head was always embedded, taking as many voxels as necessary (dependent on

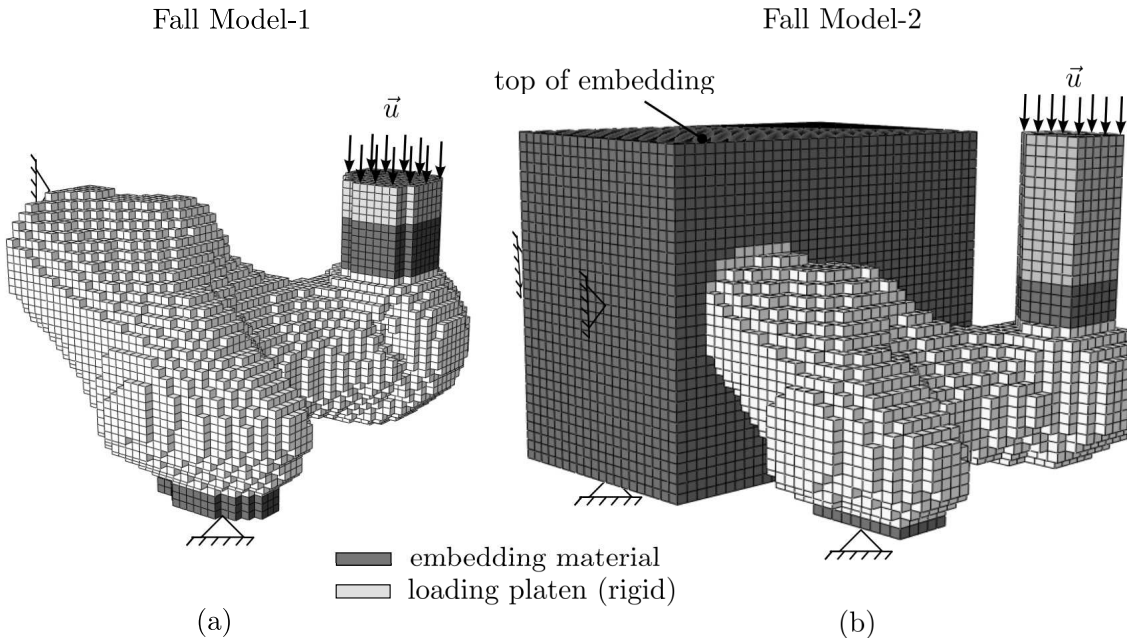

Figure 2.17: Examples of a 2 mm (a) and a 3 mm (b) mesh to simulate the fall configuration. The bottom of the embedding of the greater trochanter is fully constrained.
(a) Model-1, where the femoral shaft is cut off at the beginning of the embedding, the nodes of the resulting surface are fully constrained.
(b): Model-2, where the femoral shaft is embedded. The embedding is enlarged towards the borders of the image for easier exporting its border nodes as node sets, which are fully constrained.

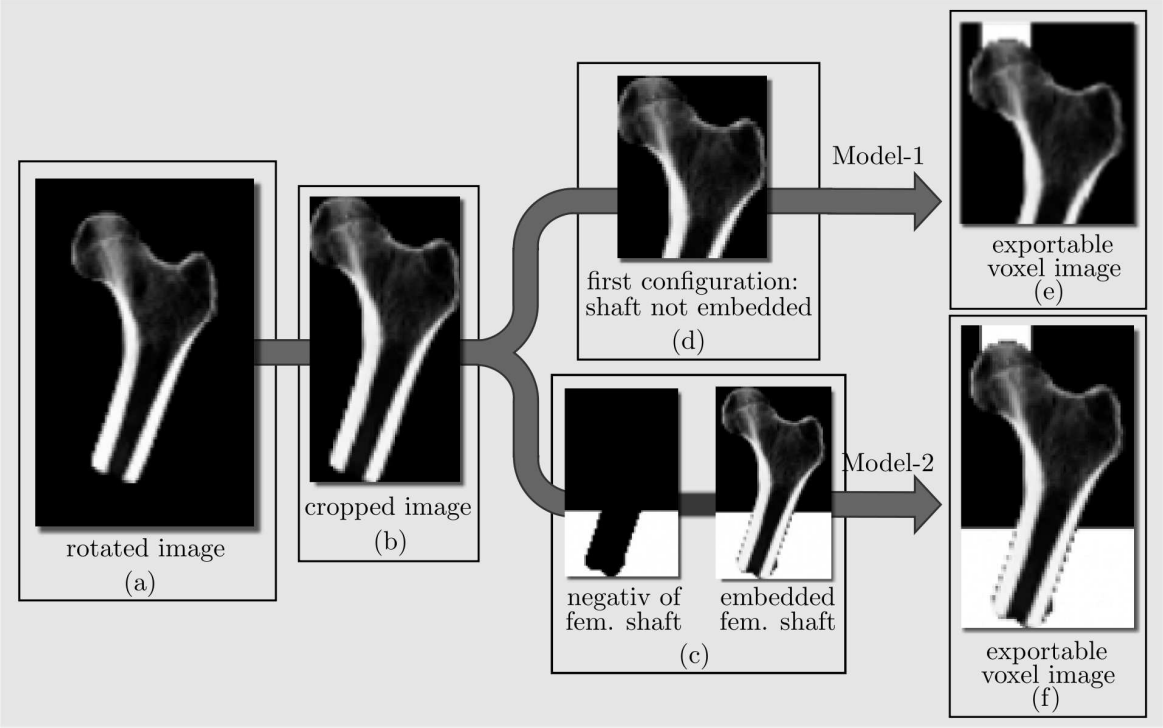

Figure 2.18: Stance configuration: First, the rotated image (a) is cropped (b). Then the shaft is either embedded (c) or cut off (b). At last, the embedding of the femoral head is added (e,f). User interaction is only needed between step (b) and step (c) and step (d), respectively.

the resolution) to represent the experimental conditions. The greater trochanter was only embedded in the fall configuration. The height of the embedding of the femoral head was chosen to represent 10 mm, which again represents the experimental conditions.

Generating an embedding was done in the following way: An image consists of the gray values corresponding to the femur (bone-voxels), and it consists of a surrounding mask (mask-voxels), which is made up of voxels with gray values equal to 0. With a function of the *mic.py*-script, it is possible to embed a given number of voxel-rows. Two problems were noticed, using this function. First, only voxels with a gray value > 0 get embedded. For example, if one wants to embed three rows of voxels, but the top row of the image only consists of masked voxels, then just two voxel rows will be embedded. To avoid such a case and to embed a *defined* number of voxel rows, it is first necessary to remove the rows, which contain only masked voxels (Figure 2.18b).

Second, *all* bone-voxels of the same row get embedded. In the stance configuration, this is no problem, since the femoral head is the only part of the femur, which is extending to the border of the image. However, in the fall configuration, other parts of the femur would first

get embedded (Figure 2.19). Therefore, generating the models of the fall configuration took additional steps and was, therefore, more complicated.

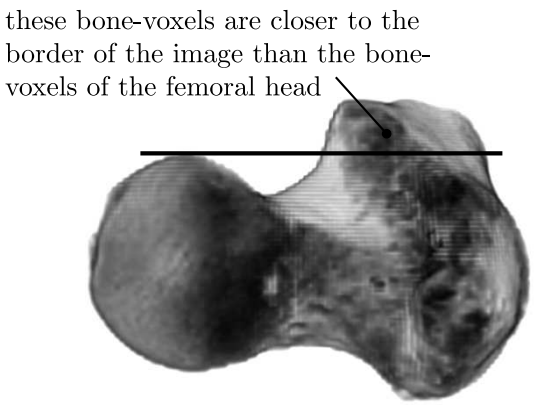

Figure 2.19: This figure illustrates the problem of embedding the femoral head in the fall configuration.

Generating the models for the stance case was done in an almost fully automated way: As an input, the developed script only needs the size in voxels of the cropped image (Figure 2.18b). This information is used for cutting off the part of the image, which is containing the shaft that is embedded (Figure 2.18d). For the generation of Model-1, the next step was to embed the femoral head. For the generation of Model-2, the cropped part containing the shaft, that should be embedded, was of further use: All gray values of this part were set to 255. Then, the gray values of the original image were added, and all gray values not equal to 255 were set to 0. This way, a negative of the femoral shaft was created (Figure 2.18c).

As a next step, this image could be added to the original one, having a femur, whose shaft is embedded, as a result. Now, the embedding of the femoral head could be added. Taking a look at Figure 2.18e, one detects dark voxels between embedding and femoral shaft. These voxels have low gray values and are a result of the partial volume effect.

The generation of Model-3 (Figure 2.16c) needed one more step than Model-2. Before creating the negative of the femoral shaft, the embedding was first rotated and then translated (the origin of the rotation did not coincide with the shaft axis). For the translation it was necessary to measure the required translation-length manually. This was only done once to investigate the influence of this more precisely modeled embedding.

As mentioned above, generating the models of the fall configuration was more complicated and needed more user interactivity: The femoral head and the greater trochanter could only be embedded, when they were separated from the remaining image (Figure 2.20b), which required additional user-interactivity. To isolate the femoral head and greater trochanter,

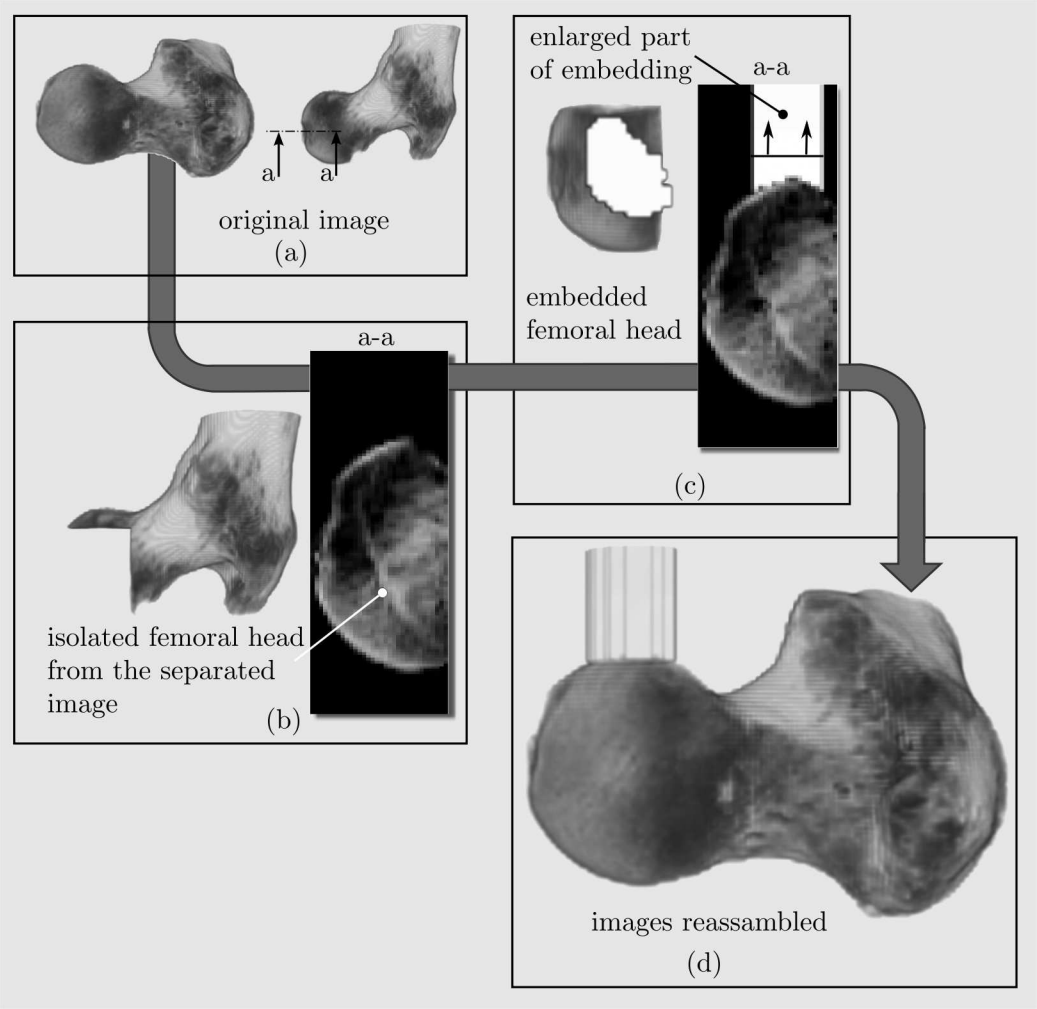

Figure 2.20: Fall configuration: The femoral head is separated (b) from the original image (a). Then it can be embedded (c) and reassembled (d) with the original image.

it was necessary to define their dimensions. In the separated image, the embedding could then be added (Figure 2.20c). Afterwards, the two images were reassembled, resulting in the final image (Figure 2.20d). Furthermore, the created embedding of the femoral head did not touch any border of the image, which would not make it possible to automatically export a cross section of the embedding as a node set. However, this was necessary to apply the boundary conditions. Therefore, the embedding was enlarged with voxels corresponding to a rigid material to the border of the image (Figure 2.20c). Embedding the femoral shaft was done in the same way as in the stance configuration.

Having done the voxel processing, the voxel images were exported to Abaqus - input files.

Figures 2.16 and 2.17 show examples of the resulting meshes, representing both loading scenarios. As will be described in the next session, material properties were assigned to every voxel, depending of its gray value. Constraints could be assigned using the automatically exported node sets.

2.8.2 Material Properties

The embedding material (PMMA) was modeled as a linear elastic, homogeneous and isotropic material with Young's modulus of 1263.5 MPa and Poisson's Ratio of 0.3 [8]. The enlarged embedding material was modeled as an approximative rigid body with a Young's modulus of 2×10^{11} MPa.

Due to the low resolution, no difference was made between cortical and trabecular bone. Its properties were modeled using the density-based (BV/TV) and fabric-based constitutive law that is described in section 1.3.4. The model was simplified by assuming cubic symmetry: The eigenvalues of the fabric tensor $\mathbf{M}$ (m_1, m_2, m_3) were set to 1, and fabric wasn't calculated.

The compliance tensor is now described by the following equation:

$$\mathbb{E} = \begin{bmatrix} E_{11} \\ E_{22} \\ E_{33} \\ \sqrt{2}E_{23} \\ \sqrt{2}E_{31} \\ \sqrt{2}E_{12} \end{bmatrix} = \begin{bmatrix} \frac{1}{\epsilon} & -\frac{\nu_0}{\epsilon} & -\frac{\nu_0}{\epsilon} & 0 & 0 & 0 \\ -\frac{\nu_0}{\epsilon} & \frac{1}{\epsilon} & -\frac{\nu_0}{\epsilon} & 0 & 0 & 0 \\ -\frac{\nu_0}{\epsilon} & -\frac{\nu_0}{\epsilon} & \frac{1}{\epsilon} & 0 & 0 & 0 \\ 0 & 0 & 0 & \frac{1}{2\mu} & 0 & 0 \\ 0 & 0 & 0 & 0 & \frac{1}{2\mu} & 0 \\ 0 & 0 & 0 & 0 & 0 & \frac{1}{2\mu} \end{bmatrix} , \tag{2.4}$$

with

$$\begin{aligned} \epsilon &= \epsilon_0 \rho^k , \\ \mu &= \mu_0 \rho^k , \end{aligned} \tag{2.5}$$

where ϵ_0, ν_0, and μ_0 are the elastic modulus, Poisson's ratio and shear modulus of the isotropic poreless bone material. These values were extrapolated from the results of multiaxial experimental testing of wet trabecular bone biopsies [58]:

$$\begin{aligned} \epsilon_0 &= 2974.0\,\text{MPa} , \qquad & \mu_0 &= 623.0\,\text{MPa} , \\ \nu_0 &= 0.181 , \qquad & k &= 0.972 . \end{aligned} \tag{2.6}$$

The material properties do not depend on fabric anymore:

$$\begin{aligned} \sigma_{ii}^{\pm} &= \sigma_0^{\pm} \rho^p \ , \\ \chi_{ij}^{\pm} &= \chi_0^{\pm} \ , \\ \tau_{ij} &= \tau_0 \rho^p \ , \end{aligned} \tag{2.7}$$

σ_0^+ and σ_0^- (the uniaxial tensile and compressive strengths), χ_0^+ and χ_0^- (the tension and compression stress interaction coefficients), and τ_0 (the shear strength) were also taken from Ref. [58]:

$$\begin{aligned} \sigma_0^+ &= 40.69\,\text{MPa} \ , & \chi_0^+ &= -0.288 \ , \\ \sigma_0^- &= 55.22\,\text{MPa} \ , & \chi_0^- &= 0.310 \ , \\ \tau_0 &= 23.10\,\text{MPa} \ , \\ p &= 1.298 \ . \end{aligned} \tag{2.8}$$

2.8.3 Evolution of Damage and plastic Yield Criteria

The description of the damage evolution was adopted from Ref. [65], which is a slightly changed description of damage evolution by Garcia et al. [22]: Plasticity was turned off

$$Y^p(\mathbf{S}^p, D) := \sqrt{\mathbf{S}^p : \mathbb{E}\mathbf{S}^p} \ , \tag{2.9}$$

and the damage hardening function in Equation 1.9 was reformulated: The exponential damage hardening law was modified to

$$r^D(D) = 1 - (1 - \alpha)e^{-kD} \ , \tag{2.10}$$

where k is the elasticity exponent of Equation 2.6 and α is the ratio of the yield to the ultimate stress, which was selected to be 2/3 [65].

$\mathbb{F}^{\pm}$ is the fourth-order tensor, formulated in terms of tensile (+) and compressive (-) domains,

which was now (regarding the assumed cubic symmetry) defined by

$$\mathbb{F} = \begin{bmatrix} \frac{1}{\sigma_0^{\pm 2}\rho^{2p}} & -\frac{\chi_0^{\pm}}{\sigma_0^{\pm 2}\rho^{2p}} & -\frac{\chi_0^{\pm}}{\sigma_0^{\pm 2}\rho^{2p}} & 0 & 0 & 0 \\ -\frac{\chi_0^{\pm}}{\sigma_0^{\pm 2}\rho^{2p}} & \frac{1}{\sigma_0^{\pm 2}\rho^{2p}} & -\frac{\chi_0^{\pm}}{\sigma_0^{\pm 2}\rho^{2p}} & 0 & 0 & 0 \\ -\frac{\chi_0^{\pm}}{\sigma_0^{\pm 2}\rho^{2p}} & -\frac{\chi_0^{\pm}}{\sigma_0^{\pm 2}\rho^{2p}} & \frac{1}{\sigma_0^{\pm 2}\rho^{2p}} & 0 & 0 & 0 \\ 0 & 0 & 0 & \frac{1}{2\tau_0^2\rho^{2p}} & 0 & 0 \\ 0 & 0 & 0 & 0 & \frac{1}{2\tau_0^2\rho^{2p}} & 0 \\ 0 & 0 & 0 & 0 & 0 & \frac{1}{2\tau_0^2\rho^{2p}} \end{bmatrix}. \tag{2.11}$$

2.8.4 Simulation

Only vertical displacements were allowed to the border nodes of the loading platen ($\vec{u}$ in Figures 2.16 and 2.17), which were applied incrementally. Any horizontal displacements of the loading platen were neglected. Boundary conditions were set in accordance to the experiments: In Model-1 (Figure 2.16a), where the embedding of the shaft was not simulated, all boundary nodes of the shaft were fully constrained. In Model-2 (Figure 2.16b), the boundary nodes of the femoral embedding were fully constrained, with one exception concerning the fall configuration: There, the nodes of the top-surface of the embedding ("top of embedding" in Figure 2.17b) could not be constrained automatically. That is because these nodes would share the same automatically exportable nodeset with the nodes of the loading platen, although they require different boundary conditions. Therefore, the constraint of these nodes was neglected. The disregard of this constraint was investigated in one case, where the constraint was added manually with a pre-processor (*Abaqus 6.9, Simulia, Dassault Systemes, Velizy-Villacoublay, France*) and did not show a strong influence.

The nonlinear static analysis was done using Abaqus 6.9 on a computer with 4 Intel Xenon 5160 processors and 64 GB RAM. The material behavior was defined for the solver as a user-defined material (UMAT). The FE-models varied significantly in size, Table 2.3 compares the number of nodes, CPU time and memory requirements of the different models, taking one left femur (stance configuration) as an example.

The force of the force-displacement curve was calculated by taking the sum of the axial reaction forces in the nodes of the top surface of the loading platen. The mean displacement was also computed from the nodes of the top surface. Stiffness and compliance were calculated using the total reaction force and the mean displacement after the first increment (0.01-0.04 mm). Femoral stiffness (C^{exp}) and compliance ($K^{exp} = 1/C^{exp}$) were identified by

Table 2.3: Number of nodes and system requirements of different models describing the stance configuration of a left femur (Figure 2.16).

	Model-1			Model-2		
	1 mm	2 mm	3 mm	1 mm	2 mm	3 mm
Number of nodes	170,243	23,412	7,489	-	69,707	24,020
CPU time	24.4 h	48.5 min	6.5 min	-	6.16 h	38.4 min
Memory requirement [MB]	15,111	1,122	275	-	4,245	1,113

taking the maximal slope of the force-displacement curve prior to failure. Calculating the maximal slope was done similar to Ref. [33]. The curve was divided into intervals representing displacements of 0.2 mm. Then linear regression analysis was used to fit lines through the data points of each interval.

Ultimate Force (F_U^{exp}) was defined as the maximum force achieved [33]. Concerning the Model-2 with the 2 mm-resolution, the calculations of the fall configuration stopped converging little before the tangent of the force displacement curve became horizontal. Therefore, F_U^{FE} was predicted by approximating the force-displacement curve by a polynomial of forth order and taking its maximum.

To investigate the influence of the compliance of the actuator, grip and loading platen, the data captured by the MTS-system and the motion-capture system were compared: First, the compliance was measured with the MTS-system, whose measurement represents the whole structure. Second, the compliance was measured using the displacement data of a marker of the motion-capture system, which was glued to the loading platen. This way, the compliance was measured without accounting for the stiffness of actuator, grip and most of the loading platen.

The influence of resolution was investigated by facing the force-displacement curves of similar models, where only the resolution varied from 1 mm to 3 mm. Above all, the influence of the embedding of the femoral shaft was shown.

Some more words concerning the modeling of the embedding: No contact condition was defined describing the contact between bone and embedding material, and no sliding was allowed at the interface bone-embedding-material. To evaluate qualitatively the physical correctness of this embedding-model, markers were placed on the femoral shaft, closely above the embedding. The displacement data of these markers were then compared with the predicted displacements.

3 Results

3.1 Experimental Tests

Six femurs were tested until failure: Three left femurs in the stance configuration and the remaining three right femurs in the fall configuration. The results for one of the six tests (stance-load case, ID=68FL) are missing due to an acquisition problem for load. Also, the acquisition of the motion-capture system failed in one case (stance-load case, ID=63MR). Figures 3.1 and 3.2 show the measured force-displacement curves of the fall configuration and stance configuration, respectively. Ultimate Force ranged from 2997 N to 3570 N in the fall configuration, and from 9912 N to 10210 N in the stance configuration (Table 3.4). The compliance, derived from the displacement data of the marker, which was glued on the loading platen, ranged from 0.651 mm/kN to 0.835 mm/kN for the fall configuration. Concerning the stance configuration, only the data of one femur (femur ID: 76FL) were available, whose compliance amounted to 0.111 mm/kN (Table 3.4).

All but one force-displacement curves, that are shown in Figures 3.1 and 3.2, were created by taking the displacement data of the loading platen, captured by the motion capture system. Only the force-displacement curve in Figure 3.2a was created using the data of the MTS-system, because the data acquisition of the motion-capture system failed in this case. Hence, this force-displacement curve also includes the compliance of actuator, grip and loading platen.

When comparing the force-displacement curves derived from the two systems (motion-capture system and MTS-system), the derived compliances differed significantly. Based on the compliance derived by the motion-capture system, the compliance increased from 6.6 % up to 20.8 %, depending on the femur tested, being smaller, when measured with the motion-capture system.

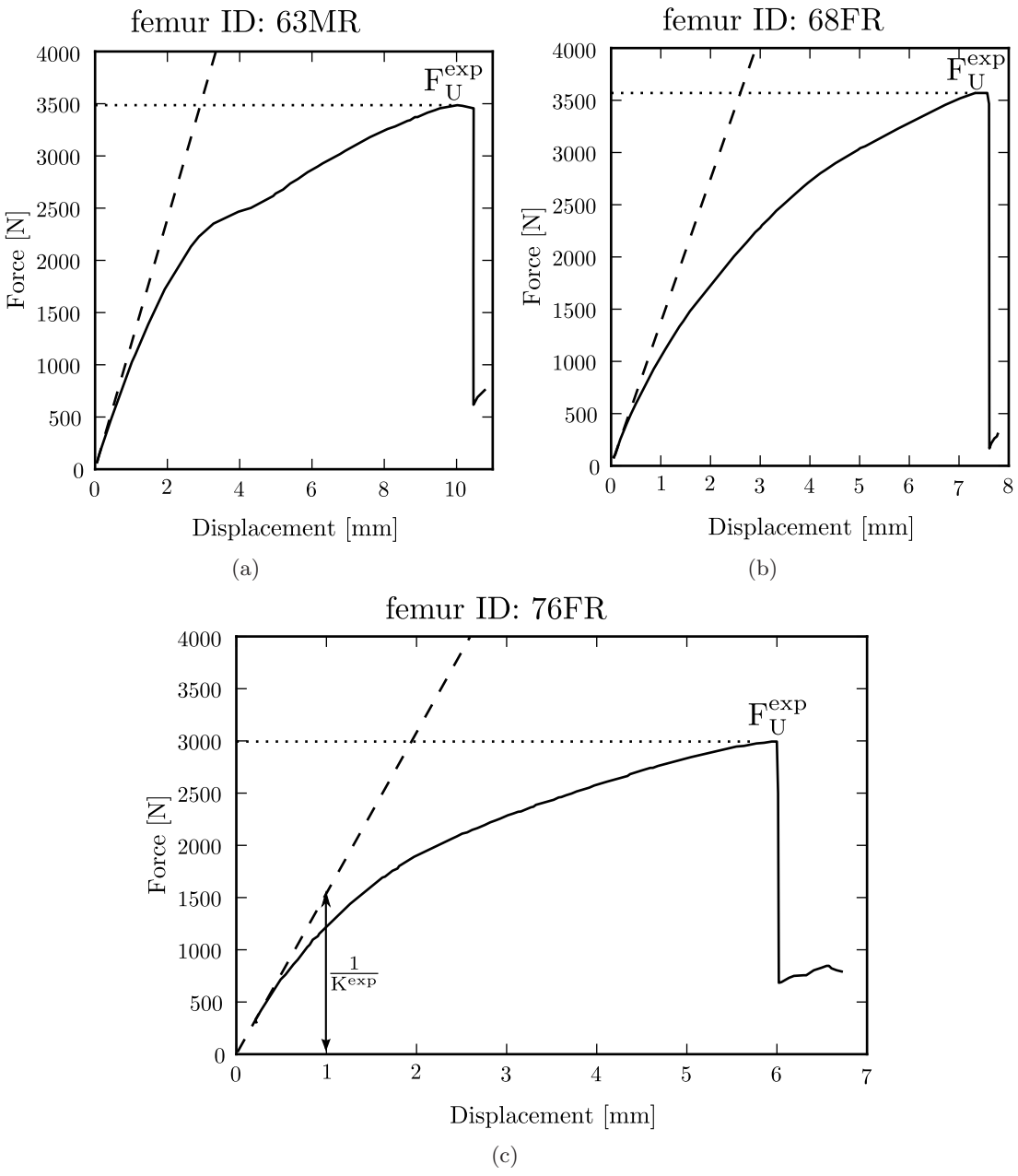

Figure 3.1: Experimental force-displacement curves of the falling configuration. Displacement data is taken from the motion-capture system. Figure (a), (b) and (c) represent pertrochanteric multifragmentary fractures (31-A2).

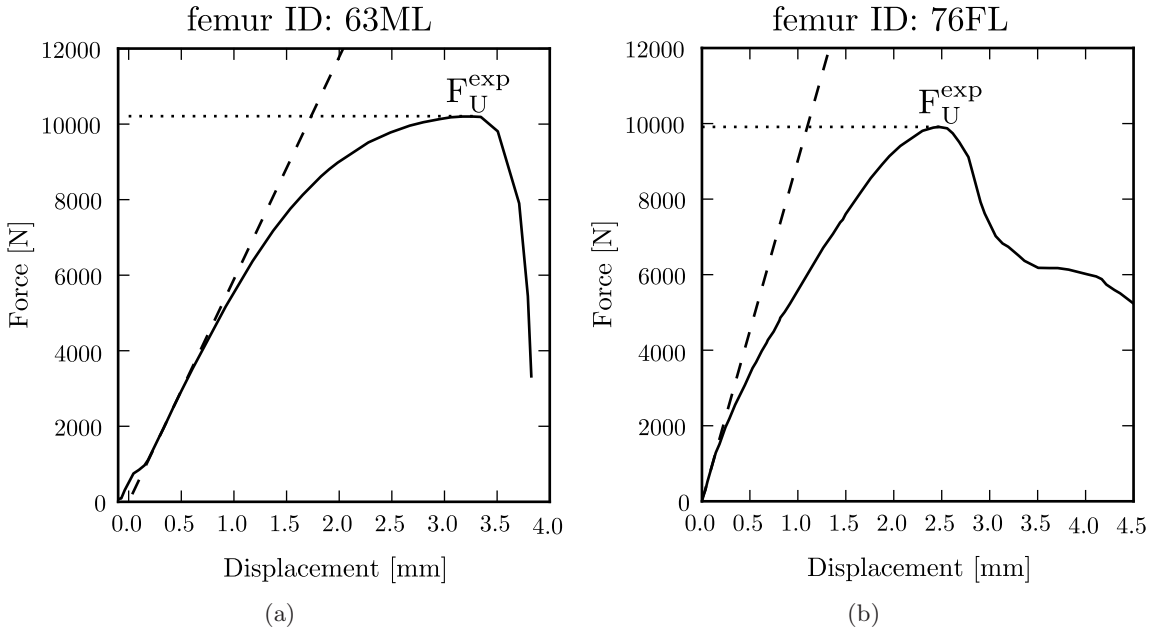

Figure 3.2: Experimental force-displacement curves of the stance configuration.
(a) Displacement data is taken from the MTS-system. The force-displacement curve represents a transcervical fracture (31-B2).
(b) Displacement data is taken from the motion-capture system. The force-displacement curve represents a subcapital fracture (31-B3).

Table 3.1: Fracture patterns of the tested femurs.

Femur ID	Fracture type	
63ML	transcervical (31-B2)	left femur
68FL	subcapital, with slight displacement (31-B1)	left femur
76FL	subcapital, displaced, nonimpacted (31-B3)	left femur
63MR	pertrochanteric multifragmentary (31-A2)	right femur
68FR	pertrochanteric multifragmentary (31-A2)	right femur
76FR	pertrochanteric multifragmentary (31-A2)	right femur

Classification according to AO groups and types.

Fracture locations were not examined radiographically. However, the right femurs (fall-loading condition) showed typical torsional fractures and were all identified as pertrochanteric fractures (31-A2) (Figure 3.12; Table 3.1). The fractures of the left femurs (stance-loading condition) were identified as either subcapital fractures (2 cases: 31-B1 and 31-B3) or transcervical fracture (31-B2) (Figure 3.11; Table 3.1). All the induced fractures were shown to an orthopedic surgeon, who confirmed that they were similar to the ones that occur in vivo.

3.1.1 Testing Setup

To check the functionality of the testing setup, the applied markers of the motion-capture system were used to measure any movements of the frame. The positions of the markers are shown in Figure 2.11. Three of them were placed on the inclined block, and two on each translation plate. The following results are taken from testing the femur "76FL" (stance configuration), which are similar to the results of the other tests. The standard deviations of the values in load direction, which were calculated from the data points that were captured before loading, were approximately 0.004 mm. The maximal displacements of the inclined block were approximately 0.05 mm (left side) and 0.06 mm (right side) in load direction. The marker on the loading platen showed a horizontal movement. When the loading platen moved 5 mm in vertical direction, the displacement's magnitude in horizontal direction amounted to 1,9 mm, which corresponds to a deviation of 20.8 degrees.

Table 3.2: Impact of resolution on the numerical results.

	Compliance [mm/kN]	F_U^{FE}
1 mm	0.181 (≙100 %)	6820 (≙100 %)
2 mm	0.169 (≙93.4 %)	7284 (≙106.8 %)
3 mm	0.165 (≙91.2 %)	7201 (≙105.6 %)

Embedding of shaft not modeled (Model-1), femur ID: 76FL

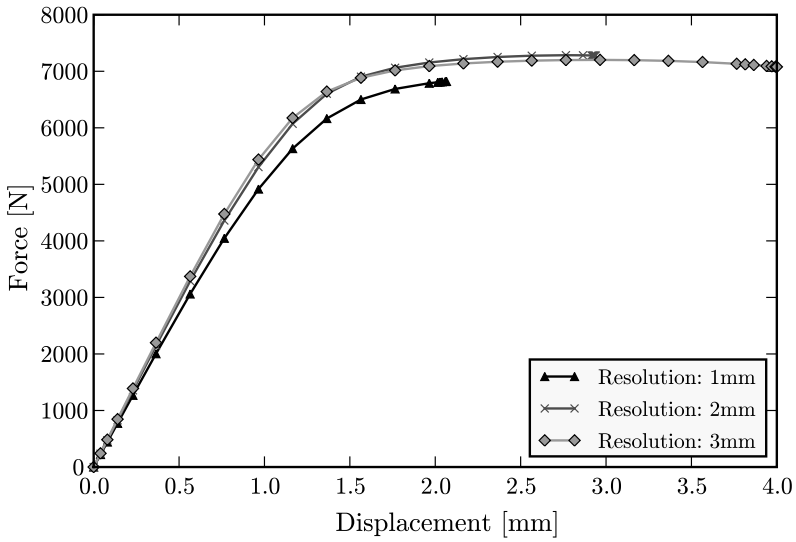

Figure 3.3: Impact of resolution on the numerical results, taking the femur "76FL" as an example (Model-1).

3.2 Nonlinear FE

Nonlinear FE analysis was done for all femurs. First, the influence of the resolution of the FE-models on the results was investigated. Figure 3.3 shows the resulting force-displacement curves of one femur (femur ID: 76FL, Model-1), where only the resolution varies from approximately 1 mm to 3 mm. The ultimate force increased by 6.8 %, the compliance decreased by 6.6 %, when comparing the 1 mm-resolution with the 2 mm-resolution (Table 3.2). The simulations with the 1 mm-resolution failed in two cases: The calculations stopped converging in approximately linear parts of the force-displacement curves before the peak of the force-displacement curve was reached.

Evaluating the prediction of fracture location is possible for all resolutions. Figure 3.4 shows

damage plots of one femur ("76FL"), modeled with different resolutions: The predicted fracture location is similarly displayed by all models.

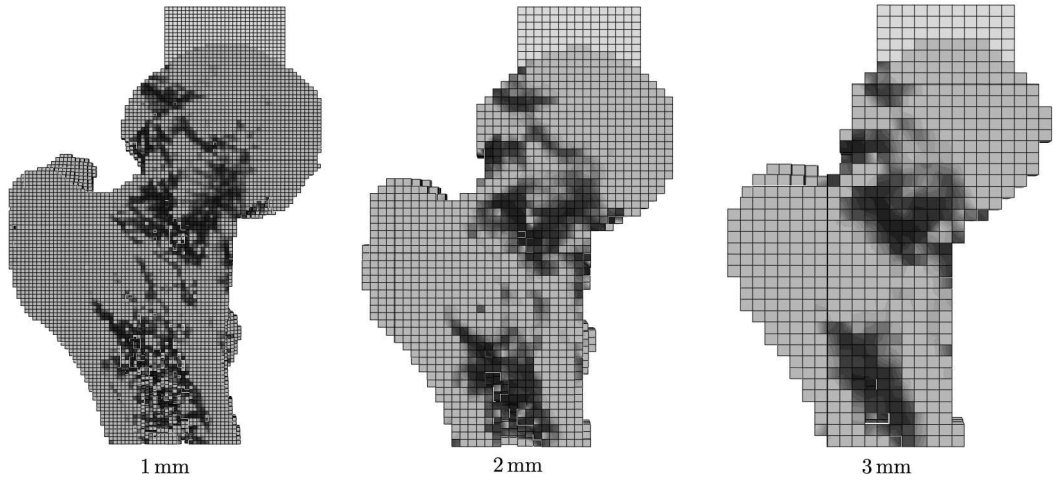

Figure 3.4: Damage plots, showing the results of a 1 mm- (left), 2 mm- (middle) and 3 mm-model (right) of the femur "FL76" (Model-1). Values were taken at the increment representing the maximal displacement of the loading platen of the 1 mm-model.

Figure 3.5 and Table 3.3 show the effect of modeling the embedding of the femoral shaft: Modeling the embedding had an impact on the compliance, which increased by 11.5 %, while the ultimate force changed only slightly ($< 1\,\%$). Simulating the embedding of the femoral shaft was not possible for the 1 mm-resolution due to the resulting huge number of nodes. To check the influence of the embedding in the experiments, the displacements of two markers, that were placed on the femoral shaft right above the embedding, were used as an indicator and compared to the predicted displacements. Taking femur "76FL" as an example for the stance configuration, the displacements in load direction of the FE analysis were -0.253 mm and -0.114 mm, corresponding to -0.205 mm and -0.075 mm, measured in the experiments. Thereby, values were either taken from the point of F_U^{exp} or from the increment representing the same displacement of the loading platen.

Although Model-2 requires a huge computational effort compared to Model-1, the results of Model-2 with resolutions of 2 mm will be presented furthermore, accounting for the big difference of the predicted stiffness.

Due to the small number of tested specimens, the results could not be evaluated statistically. Therefore, predicted and measured values were just compared qualitatively. Resulting force-displacement curves are shown in Figures 3.6 and 3.7. Figure 3.8 and Table 3.4 show the predicted compliance (K^{FE}) and ultimate force (F_U^{FE}) with the measured values (K^{exp},F_U^{exp}).

Table 3.3: Impact of modeling the embedding of the femoral shaft on numerical results.

	Compliance [mm/kN]	F_U^{FE}
Embedding not simulated (Model-1)	0.169 (≙100 %)	7277 (≙100 %)
Embedding simulated (Model-2)	0.189 (≙111.8 %)	7233 (≙99.4 %)

Resolution: 2 mm, femur ID: 76FL

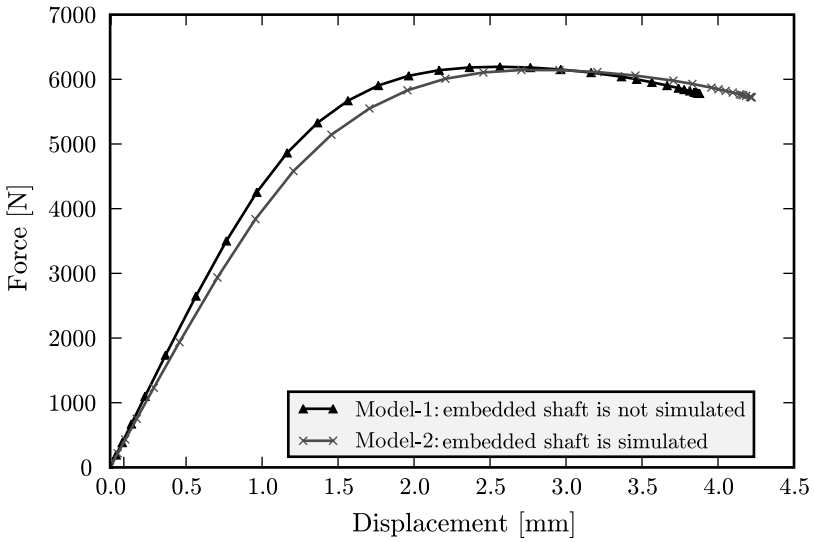

Figure 3.5: Force-displacement curves of the FE models Model-1 and Model-2, taking the femur "76FL" as an example.

Compliance, measured with the motion-capture system, was overestimated in all specimen by roughly 10 % to 70 %. Ultimate force was underestimated by roughly 30 % to 40 %, indicating a slope of a possible regression > 1. A more detailed analysis, which could investigate the correlation between measured and predicted values, would require a higher number of tested specimens.

Table 3.4: Experimental and predicted results: Predicted results are taken from Model-2 with a 2 mm-resolution.

femur ID	F_U^{exp} [N]	F_U^{FE} [N]	$K^{exp}{}_a$ [mm/kN]	$K^{exp}{}_b$ [mm/kN]	K^{FE} [mm/kN]
63MR	3,486	1,996	0.835	0.930	0.927
68FR	3,570	2,168	0.728	0.776	0.867
76FR	2,997	1,811	0.651	0.766	0.735
63ML	10,210	7,234	-	0.170	0.215
68FL	-	6,754	-	-	0.184
76FL	9,912	7,233	0.111	0.134	0.189

[a] calculated from data of motion-capture system

[b] calculated from data of MTS-system

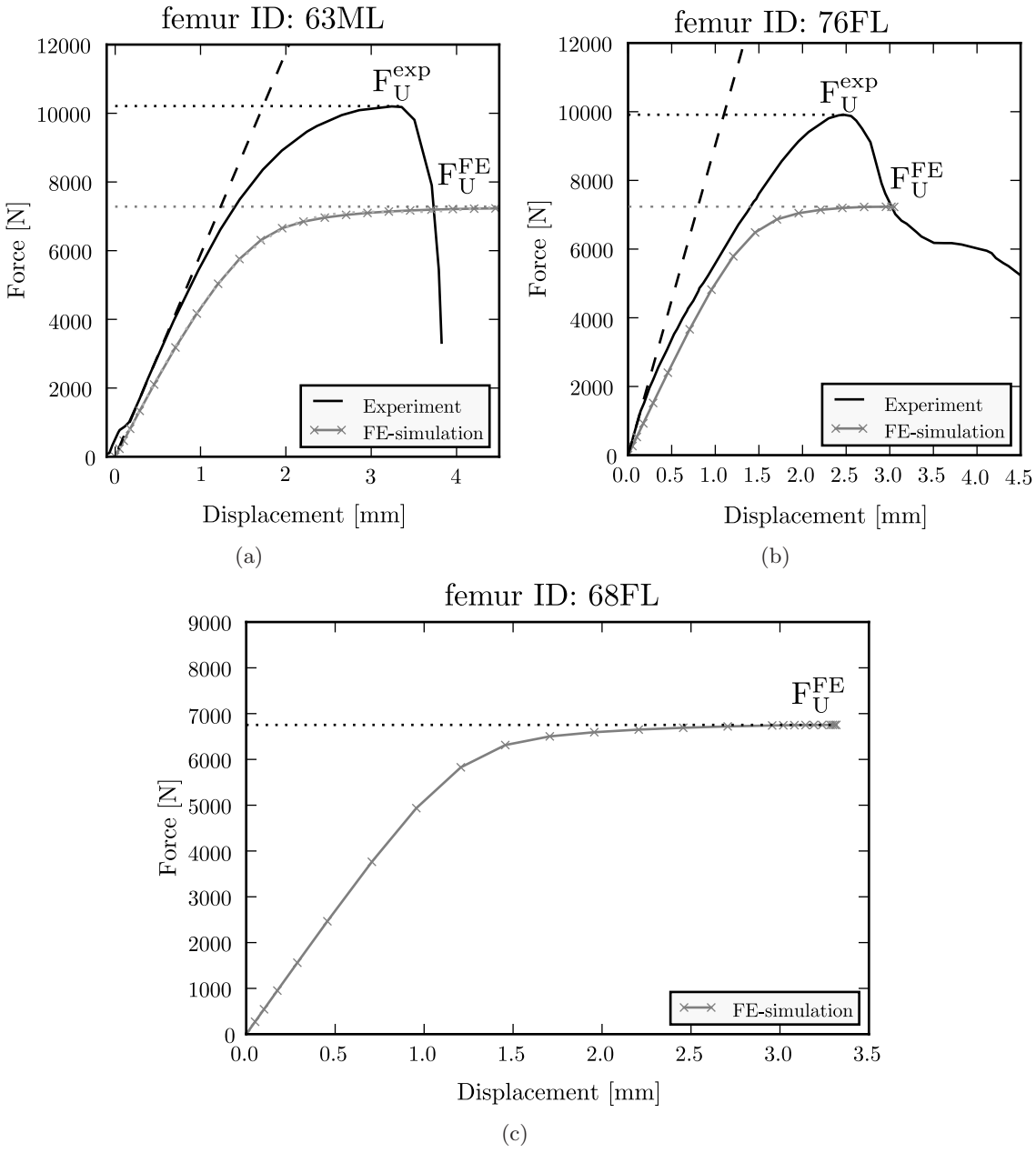

Figure 3.6: Experimental force-displacement curves and their numerical predictions (Model-2, 2 mm-resolution) from the stance configuration. For femur "68FL" (c), no experimental data were available due to a failure of the load acquisition.

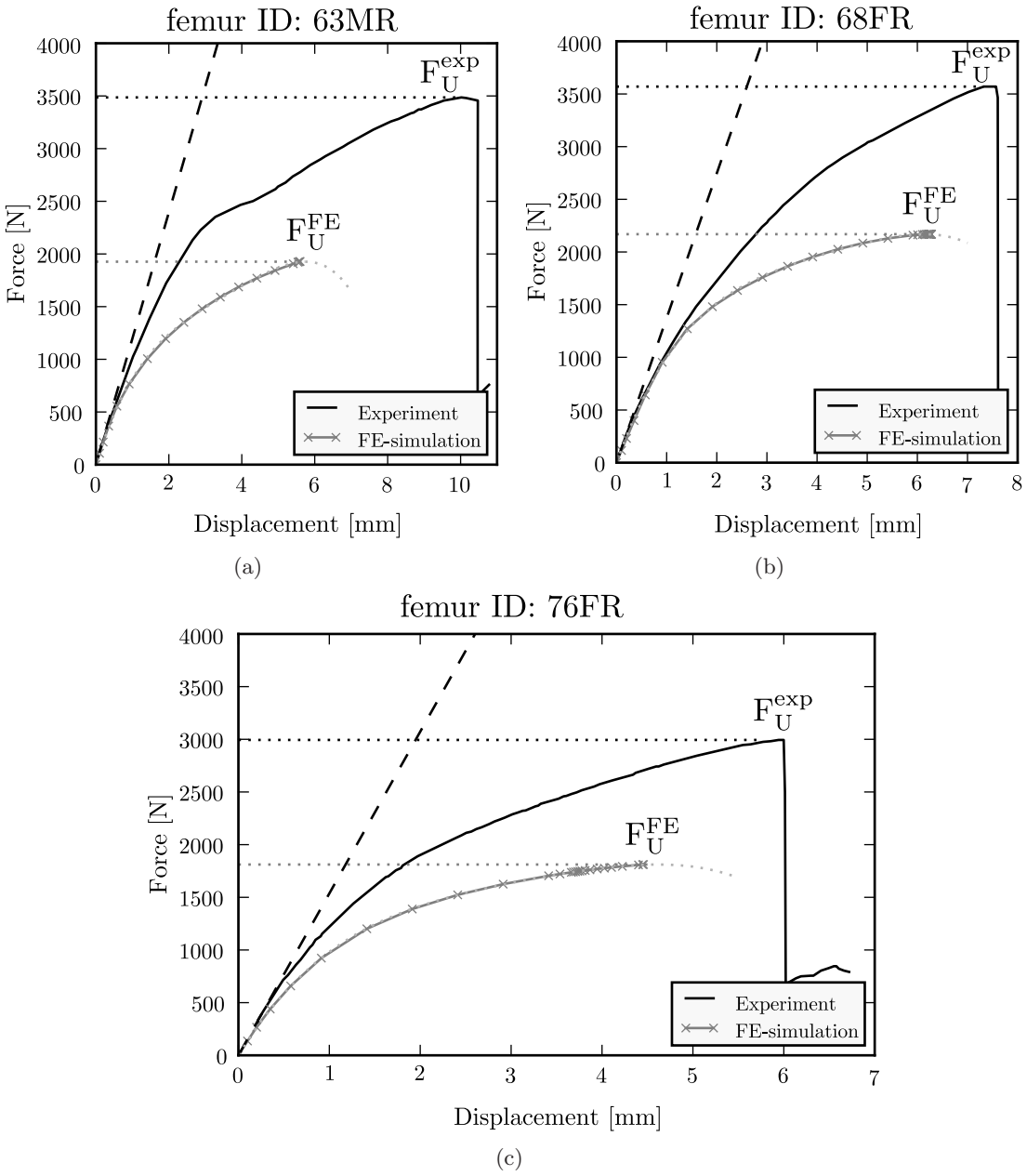

Figure 3.7: Experimental force-displacement curves and their numerical predictions (Model-2, 2 mm-resolution) from the fall configuration.

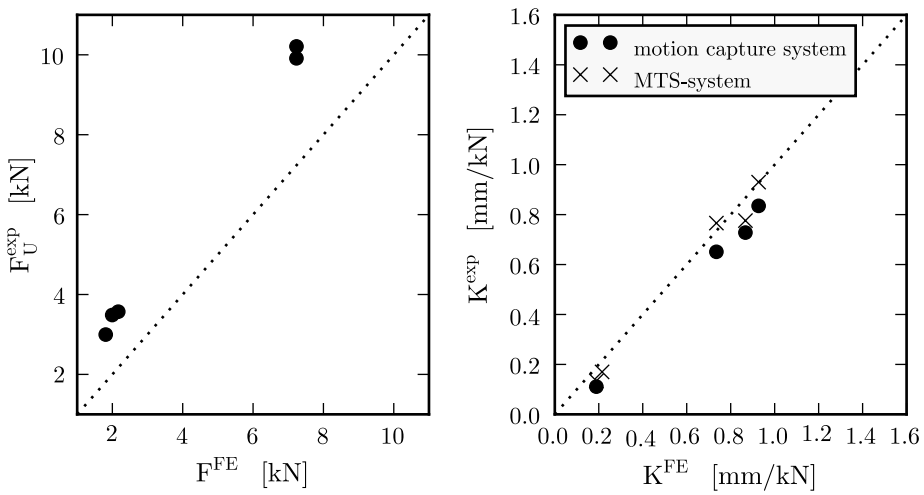

Figure 3.8: Measured ultimate force (left image) and compliance (right image) versus predicted (second model, 2 mm-resolution) ultimate force and compliance (F_U^{exp}, K^{exp} vs. F_U^{FE}, K^{FE}).

For further evaluating the numerical results, Figures 3.9 and 3.10 show the local displacements (predicted and measured) of certain points of femur "68FL", representing the stance configuration, and of femur "63MR", representing the fall configuration. The displacements of these points were measured during the experiments with the motion capture system. The numerical models predicted qualitatively well the displacements of both configurations. However, horizontal movements of the loading platen were not allowed and were, therefore, equal to 0. To investigate the measured displacements of the loading platen in x-direction, the corresponding predicted reaction forces were calculated by taking the sum of the reaction forces in the nodes of the top surface of the loading platen. The predicted, total reaction forces, which were 595 N for femur "68FL" (stance configuration) and 66 N for femur "63MR" (fall configuration), were qualitatively in agreement with the measured displacements and predicted the right directions of the loading platen's horizontal movements.

As mentioned in section 3.1.1, the measured horizontal movement of the loading platen amounted up to 1.9 mm when testing femur "76FL". Indeed, the FE-analysis of this femur showed a high total reaction force in x-direction of 1 kN.

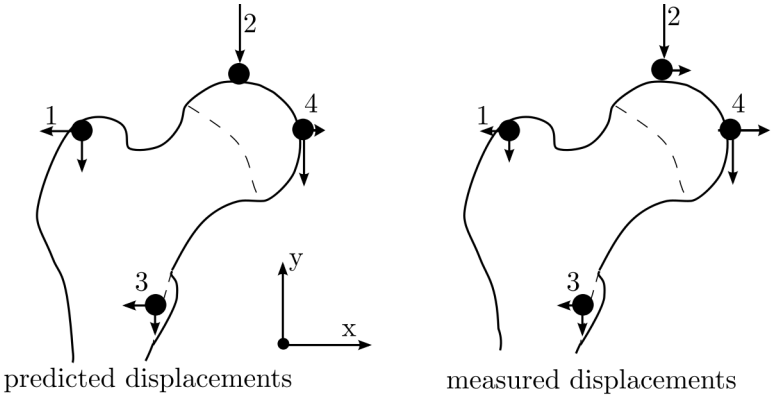

[mm]	1 x	1 y	2x	2 y	3 x	3 y	4 x	4 y
measured displacements	−0.09	−0.17	0.31	−2.18	−0.06	−0.18	0.47	−2.04
predicted displacements	−0.60	−0.55	0	−2.2	−0.31	−0.25	0.02	−2.08

Figure 3.9: Qualitative comparison of measured with predicted (second model, stance configuration, 2 mm-resolution) displacements (femur ID: 68FL), taking the experimental results from the point of F_U^{exp} and the predicted results from the increment representing the same displacement of the loading platen. The lengths of the arrows illustrate the respective displacements. The table underneath shows the actual values.

Finally, images of the produced fractures were compared with the damage plots of the

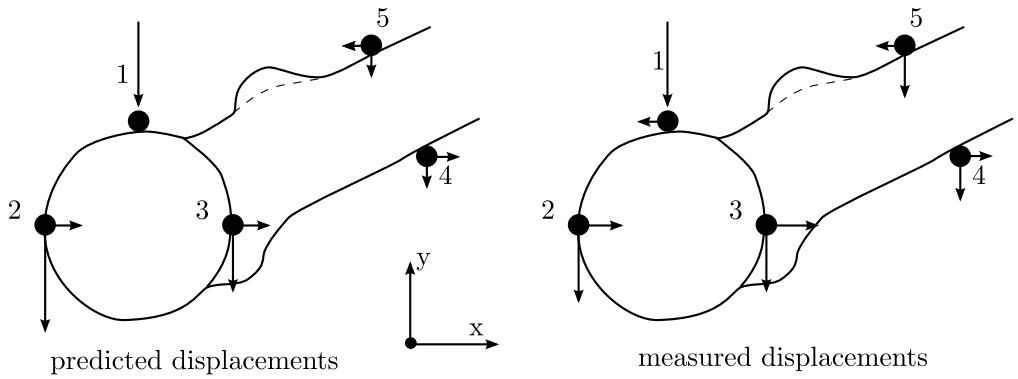

[mm]	1 x	1 y	2 x	2 y	3 x	3 y	4 x	4 y	5x	5y
measured displacements	−0.2	−5.60	1.42	−4.09	1.60	−2.90	0.23	−0.31	−0.15	−0.69
predicted displacements	0	−5.60	1.25	−6.00	1.15	−2.91	0.17	−0.14	−0.1	−0.11

Figure 3.10: Qualitative comparison of measured with predicted (second model, fall configuration, 2 mm-resolution) displacements (femur ID: 63MR), taking the predicted results of the last increment and the experimental results from the time that represents the same displacement of the loading platen. The lengths of the arrows illustrate the respective displacements. The table underneath shows the actual values.

simulations taken from the last increment (Figures 3.11 and 3.12). The predictions of the stance load cases were close to the experiments: The subcapital as well as the transcervical fractures were predicted by the FE analysis. In contrast to that, the fractures of the fall load cases were not predicted clearly. The damage plots mainly showed two damaged areas: The neck area, which is dominating, and the area around the actual fracture.

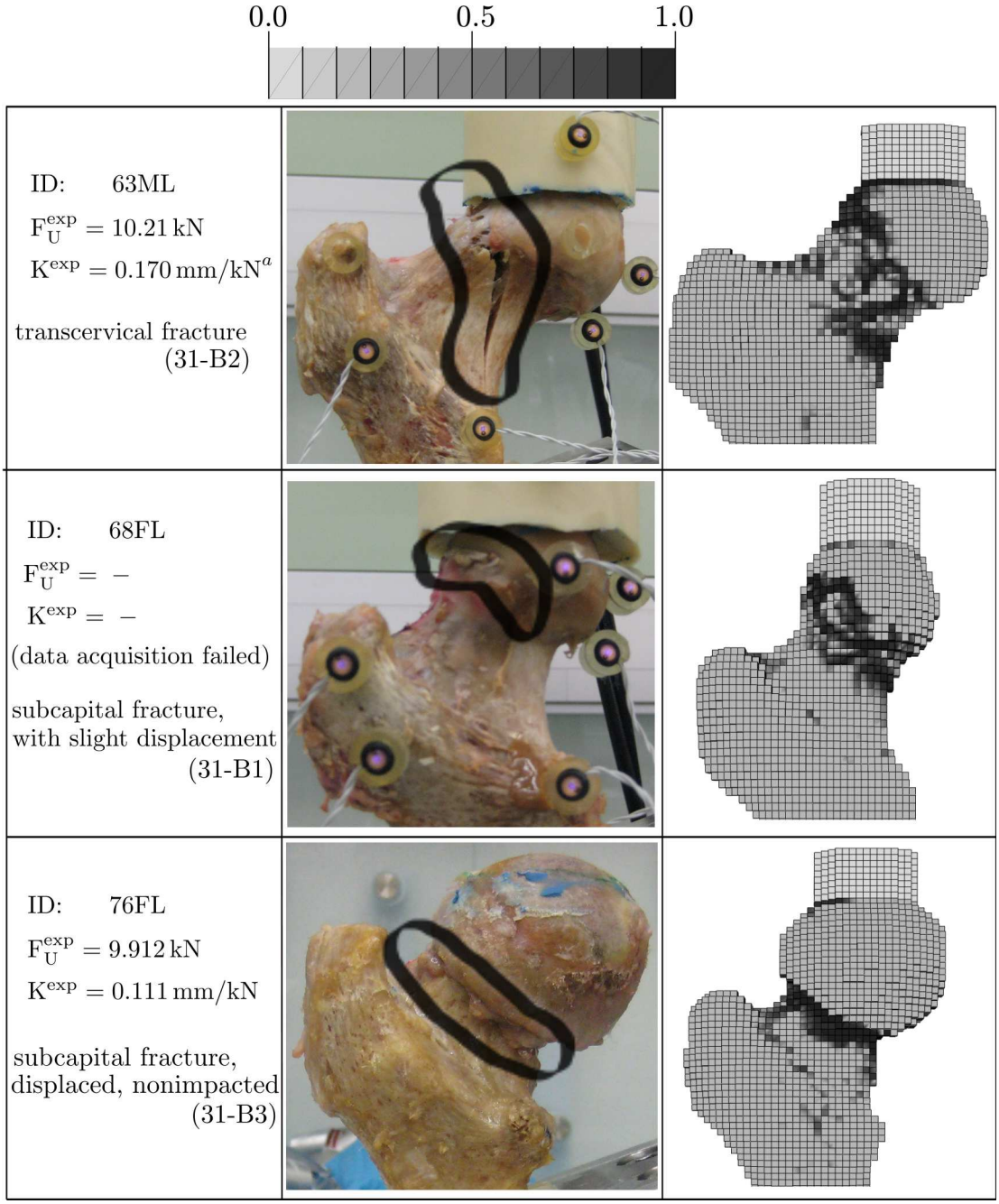

Figure 3.11: Pictures of the fractured femurs versus the damage plots of the FE analysis for the stance-loading cases. The damage plots are taken from the last increment (Model-2, 2 mm resolution), K^{exp} is derived by the data of the motion-capture system.
[a]calculated from data of MTS-system

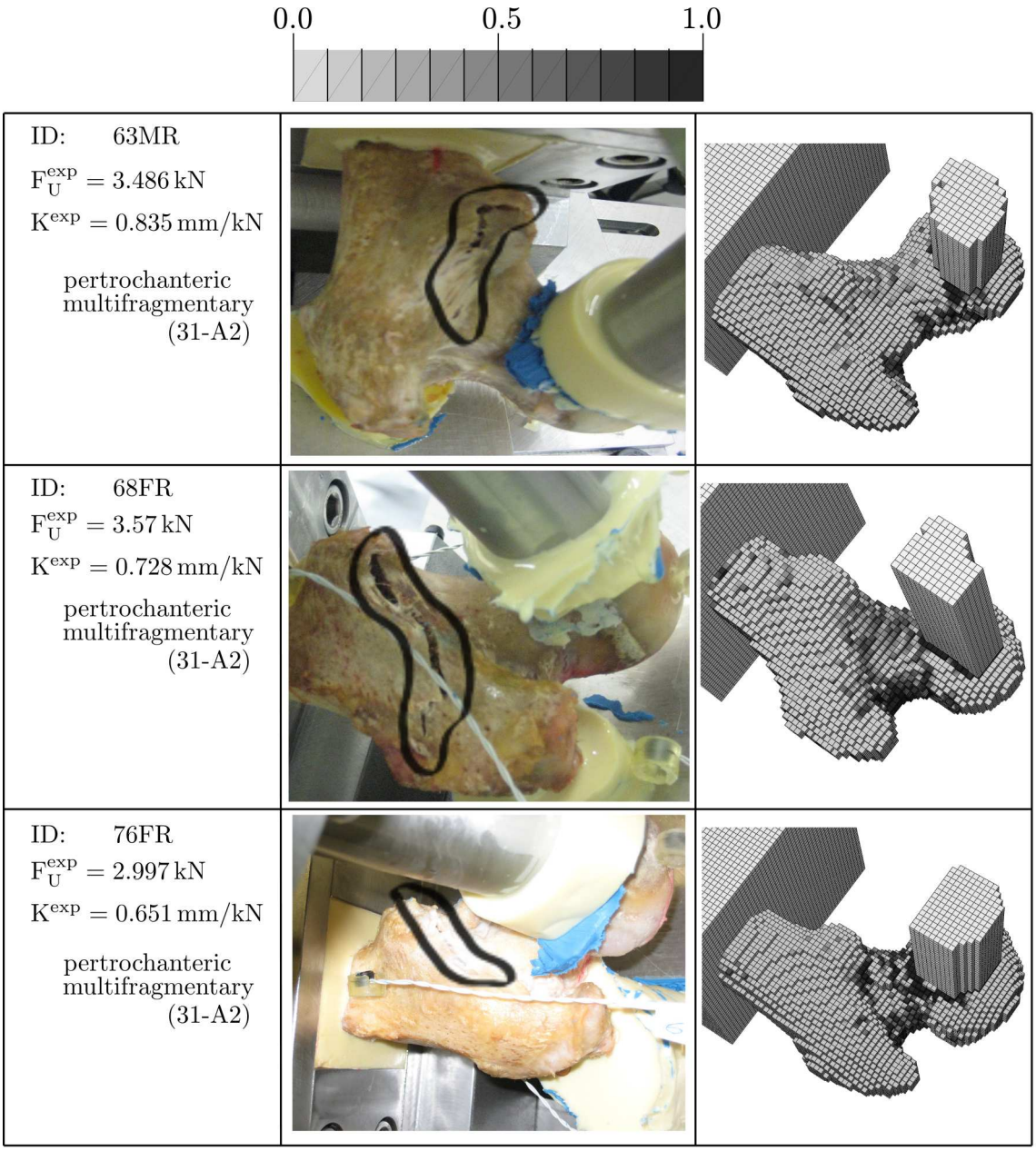

Figure 3.12: Pictures of the fractured femurs versus the damage plots of the FE analysis for the fall-loading cases taken from the last increment (Model-2, 2 mm resolution). K^{exp} is derived by the data of the motion-capture system.

4 Discussion and Conclusion

CT based FE models have given promising results. However, any new developed method needs to be validated. The purpose of this work was to do a feasibility study containing the basic procedures, that would be needed in a validation study. For this reason, a scan chamber and a testing setup were designed and manufactured. The functionality was checked by using six human femur samples. All six samples were scanned with QCT and HR-pQCT, prepared for mechanical test scenarios and loaded up to failure. Moreover, nonlinear numerical models were generated from the QCT images to simulate the experiments.

4.1 Functionality of the designed Parts

The designed scan chamber was able to scan a wide range of different sized femurs in the HR-pQCT machine. The limiting factor concerning this part of the work was the dimension of the HR-pQCT machine. The inner diameter of the scanning chamber was chosen to be 114 mm, which was the maximal diameter permitted by the HR-pQCT machine. Moreover, a maximal length of 145 mm can be scanned. These dimensions should be sufficient in the majority of cases. However, a bigger tube would be possible by scaling the current tube properly. During the scanning procedure, the tube was filled with saline solution to simulate soft tissue around the bone. This was done to be as close to an in vivo situation as possible.

The parts of the testing setup proved to be suited for testing proximal femurs: Six femurs were tested successfully, three in fall configuration and three in one-leg stance configuration. Afterwards, the movements of the frame were evaluated, whereby displacements of the inclined block were measured with the motion-capture system. Maximal displacements of the inclined block amounted to 0.065 mm. One problem was observed concerning the loading platen: Post-processing showed that vertical movement was accompanied by an undesired horizontal movement up to 1.9 mm, depending on the femur tested. Horizontal loads were not measured, but the numerical analysis predicted horizontal loads up to 1 kN. These results lead to the opinion, that the stiffness in horizontal direction of the structure, containing the actuator, grip and load cell might not be very high.

Choosing a different embedding material is an issue: The chosen embedding material has a Young's modulus of approximately 1264 MPa, which is relatively small compared to the Young's modulus of cortical bone (Table 1.1). Although the embedding material is well suited for the load-application regions, which are the femoral head and the greater trochanter, a stiffer embedding material is desirable to ensure a consistent holding of the femoral shaft. During a compression test in stance configuration (femur ID: 76FL), the top surface of the embedding moved, as a result of the low stiffness, approximately 0.12 mm in load direction. However, the stiffness is not the only problem, that was noticed. During the embedding procedure, the embedding material heated up to approximately 40° to 50 ° C, which leaded to a separation of liquid bone marrow. As a consequence, the femoral shaft was partly covered by a greasy coating, that is suspected to weaken the connection embedding-material to bone. There are several possibilities to improve the embedding of the femoral shaft: A convenient way would be to use a material with a lower hardening temperature. Another way might be to use additional tools for a better fixation. Yosibash et al. [68], for instance, used six screws for a supplementary fixation. This, however, would significantly complicate the modeling of the embedding and would, therefore, only make sense, if the resulting movements of the embedded shaft were negligible and the modeling of the shaft was not necessary.

4.2 Experiments and Numerical Analysis

The right femurs, which were all tested in the fall configuration, showed typical torsional fractures and were all identified as pertrochanteric fractures (31-A2). The fractures of the left femurs (stance-loading condition) were identified as either subcapital fractures or transcervical fractures (31-B1, 31-B2, 31-B3). These results are in good agreement with the fractures reported by Keyak [33]. For the stance configuration, she reported either subcapital fractures or oblique transcervical fractures that were approximately parallel to the shaft. Concerning the fall configuration, intertrochanteric fractures in the cervical region were reported.

When presenting the results of the experimental tests (section 3.1), it was stated, that the actuator, grip and loading platen reduced the measured compliance of the system from 6.6 % up to 20.8 %, depending on the femur tested. This difference is huge. Additionally, the overestimation of the compliance varies a lot. When comparing the force-displacement curves derived by the motion-capture system and the MTS-system, the two different displacement curves look very similar. This contradiction can be explained by the used method of calculating the compliance. 0.2 mm are a small interval to compute the stiffness. However,

the small interval is necessary, since the structure starts showing a nonlinear behavior after approximately 0.4 mm. Due to the small intervals, very small variations make a significant difference, showing that the measured compliances are rather arbitrary.

Correct modeling of the embedding is a challenge: Therefore, it was first tried to avoid embedding the femoral head by loading the femoral head of a tryout specimen with a plane surface. However, the localized force induced a non-relevant type of failure of the femoral head during experiments. Therefore, it was decided to embed the femoral head similar to Keyak [33] with a custom molded cup of PMMA. They embedded a 3 cm-diameter region, while in this study, however, it was decided to control the height the bone penetrated into the embedding, whose modeling was easier to realize.

Furthermore, modeling the embedding of the femoral shaft showed to have a considerable impact on the results and increased the predicted compliance by 11.8 %. The voxels with low BV/TV-values right next to the femoral shaft in Figure 2.18c are a result of the partial volume effect, but compensate the problem of the weakened connection between embedding-material and bone, which was described above. Evaluation of the displacements of the femoral shaft near the embedding showed qualitatively similar results of experiments and predictions in both loading configurations. Definitely, the displacements of the femoral shaft are not neglectable. In femur "63MR", for instance, the vertical displacement amounted up to 0.69 mm. In summary, the modeling of the embedding is important and represents reality better than just constraining the shaft.

Due to the small number of investigated femurs, no conclusion can be made about the ability of the used numerical model to predict stiffness, failure load etc. But this was not the goal of this work. The femoral strength of the femurs seems to be predicted more precisely than the femoral compliance. Keyak [33] using a finite element model with nonlinear material behavior and isotropic material properties, investigated the one-leg stance configuration and faced a similar problem. She predicted fracture loads within ± 2.0 kN with a 95 % confidence interval, but understated measured compliance by a factor of about 2.30 (95 % confidence interval), which shows the difficulty of predicting both fracture load and stiffness.

The predicted fracture location could easily be localized by looking at the damage parameter (D). However, fracture location was only qualitatively predicted correctly for the femurs of the stance configuration. The prediction of the fracture location in the fall configuration was unclear, indicating rather a neck fracture than a fracture of the trochanteric area. Prediction of the fracture location is again a general problem. Few studies have compared the predicted fracture location with that obtained experimentally and have clearly shown agreement. Keyak et al. [37], for instance, using a non-linear FE-model, also accounted

problems predicting fracture location and could not predict fractures in the trochanteric region. Bessho et al. [2], using a nonlinear FE-model, found an agreement of the experimental fracture site with the numerical prediction, although they only reported fractures in the subcapital region.

Measured and predicted local displacements were also investigated. In both stance configuration and fall configuration, there was a huge variation in the different predictions of the chosen displacement points. This can partly be explained by the boundary conditions, that were applied. Horizontal movements were not allowed in the FE-model. But due to occurring horizontal forces, measurements showed a horizontal movement of the loading platen, which influenced the results. The imprecise predictions are also a result of the critical points that were accounted, which will be described in the following.

First of all, choosing the right calibration function was quite a difficult task: The calibration phantom used in this study had volumes of defined partial density ranging from 0 to 204 mgHA/cm^3. A linear calibration function (HU-ρ_{QCT}) was calculated in this density range and was assumed to remain linear beyond, resulting in ρ_{QCT} values up to approximately 1600 mgHA/cm^3. Schileo et al. [60] published averaged ρ_{QCT} values extracted from cortical bone of the femoral diaphysis, ranging up to 1450 mgHA/cm^3. A similar procedure was applied in the present study to one QCT scan, resulting in an averaged ρ_{QCT} value of approximately 1400 mgHA/cm^3, which shows good agreement and confirmed us in the assumption of a uniformly valid linear HU-ρ_{QCT} calibration function. However, this uncertainty should be eliminated by using a different calibration phantom with a wider density range.

The calibration curve for the relation ρ_{QCT}-BV/TV used by Dall'Ara et al. [14] was only validated for vertebrae and assumes a BV/TV of 100 % at a ρ_{QCT} of 1059 mgHA/cm^3. However, as mentioned above, much larger ρ_{QCT} values were noticed in the present study, indicating that the calibration function is not uniformly valid for all anatomical sides. However, this point remained rather unclear. No closer information was found in literature describing maximal ρ_{QCT} values found in proximal femurs. The calibration function that was assumed in the present study (Figure 2.14) needs to be validated and probably modified, using a procedure similar to the one already used for vertebrae [13] and radius [64].

Another problem was detected when applying the material properties: They are based on experimental data measured from human trabecular bone, extrapolated to values corresponding to a BV/TV of 100 % [58]. Varga et al. [65], who used the same constitutive law to describe the material properties, but with accounting for the fabric, treated the cortical bone separately. They assigned to the cortical shell different material properties, measured

directly from experimental tests on cortical bone. Kaneko et al. [28], for example, investigated material properties of femoral cortical bone (from the diaphysis), and published the following values: $\sigma_u^- = 161.8\,\mathrm{MPa}, \sigma_u^+ = 95.6\,\mathrm{MPa}, \epsilon = 22,7\,\mathrm{GPa}$, which are more than twice as high as the extrapolated values published by Rincón-Kohli and Zysset [58]. However, cortical shell was not modeled separately in this work. This is probably the main reason for the high underestimation of failure load.

One more critical point needs to be discussed. As mentioned above, the loading platen showed an undesired horizontal movement in the experiments. This movement was a quite unexpected result and has, therefore, not been modeled. In the FE-models, any horizontal movements of the loading platen were constrained. However, this negligence could have a significant impact on the predictions, and should be corrected. One suggestion is to adapt the system to avoid transmission of horizontal force components. Cristofolini et al. [12], for instance, applied the load to the femoral head through a system of rails. Another possibility would be to adapt the FE-model. The measured displacements could be used to preset the displacements of the loading platen in the numerical analysis.

In conclusion, a testing setup and a testing chamber, which are capable of scanning and testing proximal femurs in both fall and one-leg stance configuration, were successfully designed and manufactured. The used QCT based FE models could only roughly predict fracture location, fracture load and stiffness. However, the FE models could be a powerful tool, when used in combination with HR-pQCT scans, where the cortical shell can be modeled separately. Evaluation of the presented work leaded to the following main suggestions for improvement:

- Thinking about a validation study, which includes 30 or more pairs of femurs, a fully automated FE-model generation would be useful. To accomplish this task, additional numerical tools would need to be developed.
- A different calibration phantom, covering a wider range of density, would overcome the uncertainty, if the HU-ρ_{QCT} relationship is really linear, as assumed in this work. Ideally, the calibration phantom would have inserts corresponding to trabecular as well as cortical bone.
- The calibration function for the relation ρ_{QCT}-BV/TV needs to be investigated closer and validated.
- A better fixation of the femoral shaft is desirable to ensure a consistent holding.
- The transmission of horizontal force components between loading platen and load cell should either be avoided, or the measured horizontal displacements should be modeled.

Bibliography

[1] P. Ammann and R. Rizzoli. Bone strength and its determinants. *Osteoporos Int*, 14 Suppl 3:S13–S18, 2003.

[2] M. Bessho, I. Ohnishi, J. Matsuyama, T. Matsumoto, K. Imai, and K. Nakamura. Prediction of strength and strain of the proximal femur by a ct-based finite element method. *J Biomech*, 40(8):1745–1753, 2007.

[3] W. A. Brekelmans, H. W. Poort, and T. J. Slooff. A new method to analyse the mechanical behaviour of skeletal parts. *Acta Orthop Scand*, 43(5):301–317, 1972.

[4] R. A. Brooks and G. D. Chiro. Beam hardening in x-ray reconstructive tomography. *Phys Med Biol*, 21(3):390–398, May 1976.

[5] H. T. Calis, M. Eryavuz, and M. Calis. Comparison of femoral geometry among cases with and without hip fractures. *Yonsei Med J*, 45(5):901–907, Oct 2004.

[6] D. R. Carter and W. C. Hayes. The compressive behavior of bone as a two-phase porous structure. *J Bone Joint Surg Am*, 59(7):954–962, Oct 1977.

[7] X. G. Cheng, G. Lowet, S. Boonen, P. H. F. Nicholson, P. Brys, J. Nijs, and J. Dequeker. Assessment of the strength of proximal femur in vitro: Relationship to femoral bone mineral density and femoral geometry. *Bone*, 20(3):213–218, Mar. 1997.

[8] Y. Chevalier, M. Charlebois, D. Pahr, P. Varga, P. Heini, E. Schneider, and P. Zysset. A patient-specific finite element methodology to predict damage accumulation in vertebral bodies under axial compression, sagittal flexion and combined loads. *Comput Methods Biomech Biomed Engin*, 11(5):477–487, Oct 2008.

[9] D. D. Cody, G. J. Gross, F. J. Hou, H. J. Spencer, S. A. Goldstein, and D. P. Fyhrie. Femoral strength is better predicted by finite element models than qct and dxa. *Journal of Biomechanics*, 32(10):1013–1020, Oct. 1999.

[10] A. C. Courtney, E. F. Wachtel, E. R. Myers, and W. C. Hayes. Effects of loading rate on strength of the proximal femur. *Calcif Tissue Int*, 55(1):53–58, Jul 1994.

[11] S. Cowin, Author, J. Telega, and Reviewer. *Bone Mechanics Handbook, 2nd Edition.* -, volume 56. ASME, 2003.

[12] L. Cristofolini, M. Juszczyk, S. Martelli, F. Taddei, and M. Viceconti. In vitro replication of spontaneous fractures of the proximal human femur. *Journal of Biomechanics*, 40 (13):2837–2845, 2007.

[13] E. Dall'Ara, P. Varga, D. Pahr, and P. K. Zysset. Full range calibration of local qct bmd for human vertebral body with registered micro-ct images. Submitted to Medical Engineering and Physics.

[14] E. Dall'Ara, R. Schmidt, D. Pahr, P. Varga, Y. Chevalier, J. Patsch, F. Kainberger, and P. K. Zysset. A nonlinear finite element model validation study based on a novel experimental technique for inducing anterior wedge-shape fractures in human vertebral bodies in vitro. 2009.

[15] H. der Sozialversicherungsträger. Österreichischer osteoporosebericht. *Verein Altern mit Zukunft (Hrsg)*, Wien, August 2007.

[16] T. Dorner, E. Weichselbaum, K. Lawrence, K. Viktoria Stein, and A. Rieder. Austrian osteoporosis report: epidemiology, lifestyle factors, public health strategies. *WMW Wiener Medizinische Wochenschrift*, 159(9):221–229, May 2009.

[17] T. A. Einhorn, M. Azria, and S. A. Goldstein. *Bone Fragility/The Biomechanics of Normal and Pathologic Bone*. Sandoz, Basel, Switzerland,, 1994.

[18] C. R. Ethier and C. A. Simmons. *Introductory Biomechanics From Cells to Organisms*. Cambridge University Press, 2007.

[19] K. G. Faulkner, C. E. Cann, and B. H. Hasegawa. Effect of bone distribution on vertebral strength: assessment with patient-specific nonlinear finite element analysis. *Radiology*, 179(3):669–674, Jun 1991.

[20] K. G. Faulkner, S. R. Cummings, D. Black, L. Palermo, C. C. Glüer, and H. K. Genant. Simple measurement of femoral geometry predicts hip fracture: the study of osteoporotic fractures. *J Bone Miner Res*, 8(10):1211–1217, Oct 1993.

[21] D. Garcia. *Elastic plastic damage constitutive laws for cortical bone*. PhD thesis, Ecole Polytechnique F´d´rale de Lausanne (EPFL), 2006.

[22] D. Garcia, P. K. Zysset, M. Charlebois, and A. Curnier. A three-dimensional elastic plastic damage constitutive law for bone tissue. *Biomech Model Mechanobiol*, 8(2): 149–165, Apr 2009.

[23] R. W. Goulet, S. A. Goldstein, M. J. Ciarelli, J. L. Kuhn, M. B. Brown, and L. A. Feldkamp. The relationship between the structural and orthogonal compressive properties of trabecular bone. *J Biomech*, 27(4):375–389, Apr 1994.

[24] J. S. Gregory and R. M. Aspden. Femoral geometry as a risk factor for osteoporotic hip fracture in men and women. *Med Eng Phys*, 30(10):1275–1286, Dec 2008.

[25] W. W. R. P. W. H. F. P. Gupta HS, Stachewicz U. Mechanical modulation at the lamellar level in osteonal bone. *Journal of Materials Research*, 21:1913–1921, 2006.

[26] W. C. Hayes, S. J. Piazza, and P. K. Zysset. Biomechanics of fracture risk prediction of the hip and spine by quantitative computed tomography. *Radiol Clin North Am*, 29 (1):1–18, Jan 1991.

[27] J. M. Jurist and A. S. Foltz. Human ulnar bending stiffness, mineral content, geometry and strength. *J Biomech*, 10(8):455–459, 1977.

[28] T. S. Kaneko, M. R. Pejcic, J. Tehranzadeh, and J. H. Keyak. Relationships between material properties and ct scan data of cortical bone with and without metastatic lesions. *Med Eng Phys*, 25(6):445–454, Jul 2003.

[29] J. Kanis, O. Johnell, A. Oden, H. Johansson, and E. McCloskey. Frax? and the assessment of fracture probability in men and women from the uk. *Osteoporosis International*, 19(4):385–397, Apr. 2008.

[30] T. M. Keaveny, E. F. Morgan, G. L. Niebur, and O. C. Yeh. Biomechanics of trabecular bone. *Annu Rev Biomed Eng*, 3:307–333, 2001.

[31] T. S. Keller. Predicting the compressive mechanical behavior of bone. *J Biomech*, 27 (9):1159–1168, Sep 1994.

[32] J. H. Keyak. Relationships between femoral fracture loads for two load configurations. *J Biomech*, 33(4):499–502, Apr 2000.

[33] J. H. Keyak. Improved prediction of proximal femoral fracture load using nonlinear finite element models. *Medical Engineering & Physics*, 23(3):165–173, Apr. 2001.

[34] J. H. Keyak, I. Y. Lee, and H. B. Skinner. Correlations between orthogonal mechanical properties and density of trabecular bone: use of different densitometric measures. *J Biomed Mater Res*, 28(11):1329–1336, Nov 1994.

[35] J. H. Keyak, S. A. Rossi, K. A. Jones, and H. B. Skinner. Prediction of femoral fracture load using automated finite element modeling. *J Biomech*, 31(2):125–133, Feb 1998.

[36] J. H. Keyak, S. A. Rossi, K. A. Jones, C. M. Les, and H. B. Skinner. Prediction of fracture location in the proximal femur using finite element models. *Medical Engineering & Physics*, 23(9):657–664, Nov. 2001.

[37] J. H. Keyak, T. S. Kaneko, J. Tehranzadeh, and H. B. Skinner. Predicting proximal femoral strength using structural engineering models. *Clin Orthop Relat Res*, (437): 219–228, Aug 2005.

[38] C. M. Koeck, D. L. Schwappach, F. M. Niemann, T. J. Strassmann, H. Ebner, and K. Klaushofer. Incidence and costs of osteoporosis-associated hip fractures in austria. *Wien Klin Wochenschr*, 113(10):371–377, May 2001.

[39] A. Laib, H. J. Häuselmann, and P. Rüegsegger. In vivo high resolution 3d-qct of the human forearm. *Technol Health Care*, 6(5-6):329–337, Dec 1998.

[40] T. F. Lang, J. H. Keyak, M. W. Heitz, P. Augat, Y. Lu, A. Mathur, and H. K. Genant. Volumetric quantitative computed tomography of the proximal femur: Precision and relation to bone strength. *Bone*, 21(1):101 – 108, 1997.

[41] C. M. Les, J. H. Keyak, S. M. Stover, K. T. Taylor, and A. J. Kaneps. Estimation of material properties in the equine metacarpus with use of quantitative computed tomography. *J Orthop Res*, 12(6):822–833, Nov 1994.

[42] E. M. Lochmüller, J. B. Zeller, D. Kaiser, F. Eckstein, J. Landgraf, R. Putz, and R. Steldinger. Correlation of femoral and lumbar dxa and calcaneal ultrasound, measured in situ with intact soft tissues, with the in vitro failure loads of the proximal femur. *Osteoporos Int*, 8(6):591–598, 1998.

[43] J. Lotz and W. Hayes. The use of quantitative computed tomography to estimate risk of fracture of the hip from falls. *J Bone Joint Surg Am*, 72(5):689–700, June 1990.

[44] J. C. Lotz, E. J. Cheal, and W. C. Hayes. Fracture prediction for the proximal femur using finite element models: Part i—linear analysis. *Journal of Biomechanical Engineering*, 113(4):353–360, 1991.

[45] J. A. MacNeil and S. K. Boyd. Accuracy of high-resolution peripheral quantitative computed tomography for measurement of bone quality. *Med Eng Phys*, 29(10):1096–1105, Dec 2007.

[46] E. F. Morgan, H. H. Bayraktar, and T. M. Keaveny. Trabecular bone modulus-density relationships depend on anatomic site. *J Biomech*, 36(7):897–904, Jul 2003.

[47] M. E. Müller. *The comprehensive classification of fractures of long bones*. Berlin-Heidelberg: Springer, 1990.

[48] E. S. Orwoll, L. M. Marshall, C. M. Nielson, S. R. Cummings, J. Lapidus, J. A. Cauley, K. Ensrud, N. Lane, P. R. Hoffmann, D. L. Kopperdahl, T. M. Keaveny, and O. F. in Men Study Group. Finite element analysis of the proximal femur and hip fracture risk in older men. *J Bone Miner Res*, 24(3):475–483, Mar 2009.

[49] D. H. Pahr and P. K. Zysset. A comparison of enhanced continuum fe with micro fe models of human vertebral bodies. *J Biomech*, 42(4):455–462, Mar 2009.

[50] D. H. Pahr and P. K. Zysset. From high-resolution ct data to finite element models: development of an integrated modular framework. *Comput Methods Biomech Biomed Engin*, 12(1):45–57, Feb 2009.

[51] A. M. Parfitt. The physiologic and clinical significance of bone histomorphometric data. *Bone Histomorphometry*, pages 143–224, 1983.

[52] E. Perilli, M. Baleani, C. Ohman, F. Baruffaldi, and M. Viceconti. Structural parameters and mechanical strength of cancellous bone in the femoral head in osteoarthritis do not depend on age. *Bone*, 41(5):760–768, Nov 2007.

[53] B. v. R. R. Huiskes. *Basic Orthopaedic Biomechanics*, volume 3. Lippincott Williams & Wilkins, 2005.

[54] D. T. Reilly and A. H. Burstein. The elastic and ultimate properties of compact bone tissue. *J Biomech*, 8(6):393–405, 1975.

[55] J. C. Rice, S. C. Cowin, and J. A. Bowman. On the dependence of the elasticity and strength of cancellous bone on apparent density. *J Biomech*, 21(2):155–168, 1988.

[56] B. V. Rietbergen, R. Huiskes, F. Eckstein, and P. Rüegsegger. Trabecular bone tissue strains in the healthy and osteoporotic human femur. *J Bone Miner Res*, 18(10):1781–1788, Oct 2003.

[57] B. L. Riggs and L. J. Melton. Evidence for two distinct syndromes of involutional osteoporosis. *Am J Med*, 75(6):899–901, Dec 1983.

[58] L. Rincón-Kohli and P. K. Zysset. Multi-axial mechanical properties of human trabecular bone. *Biomech Model Mechanobiol*, 8(3):195–208, Jun 2009.

[59] P. J. Rubin, P. F. Leyvraz, J. M. Aubaniac, J. N. Argenson, P. Estève, and B. de Roguin. The morphology of the proximal femur. a three-dimensional radiographic analysis. *J Bone Joint Surg Br*, 74(1):28–32, Jan 1992.

[60] E. Schileo, E. Dall'ara, F. Taddei, A. Malandrino, T. Schotkamp, M. Baleani, and M. Viceconti. An accurate estimation of bone density improves the accuracy of subject-specific finite element models. *J Biomech*, 41(11):2483–2491, Aug 2008.

[61] F. Taddei, L. Cristofolini, S. Martelli, H. S. Gill, and M. Viceconti. Subject-specific finite element models of long bones: An in vitro evaluation of the overall accuracy. *J Biomech*, 39(13):2457–2467, 2006.

[62] B. van Rietbergen, H. Weinans, R. Huiskes, and A. Odgaard. A new method to determine trabecular bone elastic properties and loading using micromechanical finite-element models. *J Biomech*, 28(1):69–81, Jan 1995.

[63] P. Varga. *Prediction of distal radius fracture load using HR?pQCT?based finite element analysis*. PhD thesis, Vienna University of Technology, 2009.

[64] P. Varga and P. K. Zysset. Assessment of volume fraction and fabric in the distal radius using hr-pqct. *Bone*, 45(5):909–917, Nov 2009.

[65] P. Varga, S. Baumbach, D. Pahr, and P. K. Zysset. Validation of an anatomy specific finite element model of colles' fracture. *J Biomech*, 42(11):1726–1731, Aug 2009.

[66] E. Verhulp, B. van Rietbergen, and R. Huiskes. Comparison of micro-level and continuum-level voxel models of the proximal femur. *J Biomech*, 39(16):2951–2957, 2006.

[67] E. Verhulp, B. van Rietbergen, and R. Huiskes. Load distribution in the healthy and osteoporotic human proximal femur during a fall to the side. *Bone*, 42(1):30–35, Jan 2008.

[68] Z. Yosibash, R. Padan, L. Joskowicz, and C. Milgrom. A ct-based high-order finite element analysis of the human proximal femur compared to in-vitro experiments. *J Biomech Eng*, 129(3):297–309, Jun 2007.

[69] Z. Yosibash, N. Trabelsi, and C. Milgrom. Reliable simulations of the human proximal femur by high-order finite element analysis validated by experimental observations. *Journal of Biomechanics*, 40(16):3688 – 3699, 2007.

[70] P. K. Zysset. A review of morphology-elasticity relationships in human trabecular bone: theories and experiments. *J Biomech*, 36(10):1469–1485, Oct 2003.

[71] P. K. Zysset and A. Curnier. An alternative model for anisotropic elasticity based on fabric tensors. *Mechanics of Materials*, 21(4):243 – 250, 1995.